Scholars' Mine

Fall 2020

The role of tectonic inheritance, plate-reorganization, and magma flare-ups in the evolution of the Sevier Orogeny

J. Daniel Quick

Follow this and additional works at: https://scholarsmine.mst.edu/masters_theses

Part of the Geology Commons

Department:

Recommended Citation

Quick, J. Daniel, "The role of tectonic inheritance, plate-reorganization, and magma flare-ups in the evolution of the Sevier Orogeny" (2020). *Masters Theses*. 7969.
https://scholarsmine.mst.edu/masters_theses/7969

THE ROLE OF TECTONIC INHERITANCE, PLATE-REORGANIZATION, AND

MAGMA FLARE-UPS IN THE EVOLUTION OF THE SEVIER OROGENY

by

JAMES DANIEL QUICK

A THESIS

Presented to the Graduate Faculty of the

MISSOURI UNIVERSITY OF SCIENCE AND TECHNOLOGY

In Partial Fulfillment of the Requirements for the Degree

MASTER OF SCIENCE

in

GEOLOGY AND GEOPHYSICS

2020

Approved by:

Dr. John P. Hogan, Advisor
Dr. Jonathan Obrist-Farner
Dr. Michael Wizevich

PUBLICATION THESIS OPTION

This thesis consists of the following article, formatted in the style used by the Missouri University of Science and Technology:

Paper I, found on pages 4–19, has been submitted to *Rock Mountain Geology*.

ABSTRACT

The temporal and spatial distribution of strain associated with the Sevier Orogeny in western North America is significantly different in the southern end of the belt, at the latitude of Las Vegas, than further to the north at the latitude of Salt Lake City. Until this study, reasons for these differences were speculative as a lack of thrust kinematic data in the intervening region hindered along strike correlation across the belt. A crystallization age of $100.18 \pm 14\ 0.04$ Ma was determined for zircons extracted from a recently recognized ash fall tuff near the base of the synorogenic Iron Springs Formation at Three Peaks, Iron County, Utah. Field relationships and this age constrain movement on the Iron Springs thrust and the end of the sub-Cretaceous unconformity in the critical intervening area to latest Albian/earliest Cenomanian. Movement on the Iron Springs thrust and other Sevier thrusts at ~100 Ma is synchronous with a period of global plate reorganization and a high convergence rate for the Farallon Plate, which led to a Cordilleran arc flare-up event, and triggered widespread thrusting across the retroarc Sevier deformation belts. Based on these results, we suggest temporal and spatial variation along the strike of the orogenic belt are inherited from variation in the thickness of the rifted Precambrian craton.

ACKNOWLEDGMENTS

TABLE OF CONTENTS

LIST OF ILLUSTRATIONS

NOMENCLATURE

Symbol	Description
TPT	Three Peaks Tuff
PL	Paragonah Lineament
SFTB	Sevier Fold Thrust Belt
MCb	Marshalll Creek breccia

1. INTRODUCTION

1.1. OVERVIEW

The Sevier Orogenic belt is extensive, spanning from Canada to Mexico, and played a profound role in the tectonic evolution of the North American Cordillera (Yonkee and Weil, 2015). The Sevier Fold and Thrust Belt (SFTB) was formed during the Jurassic to the Eocene by Farallon slab subduction, leading to hundreds of km of shorting (DeCelles, 2004).

1.2. THE MYSTERY OF ALONG STRIKE VARIATION IN THE SOUTHERN SEVIER BELT

In the southern portion of the SFTB (i.e. Utah and Nevada), thrust kinematic data is scattered, with timing well constrained in northern Utah and Nevada (DeCelles, 1994), but poorly constrained in the intervening region of southwestern Utah. At the southernmost extent of the SFTB, deformation is limited in time and space. At the latitude of Las Vegas, Sevier deformation is bracketed to the west by the (160 Ma-140 Ma) Wheeler Pass Thrust (Giallorenzo et al., 2018) and to the east by the mid-Cretaceous (99 Ma) Keystone Thrust (Fleck and Carr, 1990). To the north, deformation occurred for a much longer period of time (~ 100 Ma), across a wider region (see Fig. 1 of the paper) (DeCelles, 1994). Reasons for this along strike variation have remained elusive, due to a lack of thrust kinematic data in the intervening region.

1.3. THE FLARE-UP QUESTION

Periods of high magma production in the Sevier magmatic arc are synchronous with periods of thrust fault propagation in the Sevier deformation belt (DeCelles and Graham, 2015). During the mid-Cretaceous, a flare-up in both the North and South American Cordilleras occurred along the western flank of the continents (Ardila et al., 2019), producing voluminous magma production. Results from this study verify the temporal link between thrusting and the flare-up.

1.4. THREE PEAKS, IRON COUNTY, UTAH

The Three Peaks form a series of hills cored by Miocene quartz monzonite lacoliths (Barker, 1995). The Iron Springs thrust is exposed at the southern margin of Three Peaks and uplifts the Jurassic Co-op Creek Limestone Member of the Carmel Formation in the hanging wall (Knudsen and Biek, 2014). Along the intrusion's western margin, the stratigraphically lowest continually exposed unit is the Co-op Creek Limestone Member. The Crystal Creek Member of the Carmel Formation overlies the Co-op Creek, and, at Three Peaks, consists of alternating layers of sandstone and mudstone. The Cretaceous Marshall Creek breccia disconformably overlies the Crystal Creek Member. The Marshall Creek breccia consists mostly of large (up to 1.5 m), angular limestone clasts. It interfingers with and grades into the quartzite and limestone conglomerates of the basal Iron Springs Formation. For this reason, some workers have suggested that the Marshall Creek breccia be included in the Iron Springs Formation (Knudsen and Biek, 2014; Fillmore, 1991). The Marshall Creek breccia is interpreted to be the sedimentary response to early uplift on the Iron Springs thrust (Fillmore, 1991).

The Three Peaks Tuff, a volcanic unit first identified by this study, lies above the

Marshall Creek breccia (see paper I, Fig. 2), and field relationships show that the Three

Peaks Tuff, the Marshall Creek breccia, and the conglomerate beds of the Iron Springs

Formation are similar in age.

PAPER

I. THE ROLE OF TECTONIC INHERITANCE, PLATE REORGANIZATION, AND MAGMA FLARE-UPS IN THE EVOLUTION OF THE SEVIER OROGENY

J. Daniel Quick, John P. Hogan, Michael Wizevich, Jonathan Obrist-Farner, and James L. Crowley

ABSTRACT

The temporal and spatial distribution of strain associated with the Sevier Orogeny in western North America is significantly different in the southern end of the belt, at the latitude of Las Vegas, than further to the north at the latitude of Salt Lake City. Until this study, reasons for these differences were speculative as a lack of thrust kinematic data in the intervening region hindered along strike correlation across the belt. We determined a crystallization age of 100.18 ± 14 0.04 Ma for zircons extracted from a recently recognized ash fall tuff near the base of the synorogenic Iron Springs Formation at Three Peaks, Iron County, Utah. Field relationships and this age constrain movement on the Iron Springs thrust and the end of the sub-Cretaceous unconformity in the critical intervening area to latest Albian/earliest Cenomanian. Movement on the Iron Springs thrust and other Sevier thrusts at ~100 Ma is synchronous with a period of global plate reorganization and a high convergence rate for the Farallon Plate, which led to a Cordilleran arc flare-up event, and triggered widespread thrusting across the retroarc Sevier deformation belts. Based on these results, we suggest temporal and spatial

variation along the strike of the orogenic belt are inherited from variation in the thickness of the rifted Precambrian craton.

1. INTRODUCTION

The Sevier orogeny affected the western North American Cordillera during the late Jurassic to Eocene (Yonkee and Weil, 2015; Herring and Greene, 2016; Figure 1). The orogeny, attributed to plate convergence along the edge of western North America, telescoped the antecedent passive margin along several prominent, east-directed thrusts, resulting in at least 350 km of shortening at the latitude of central Utah (DeCelles, 2004). However, the temporal and spatial evolution of the Sevier orogenic belt varies along strike (Figure 1). Near Las Vegas, the thrust belt is restricted in time (ca. 50 My) and space (<100 km) where it is defined by the Wheeler Pass thrust (160-140 Ma; Giallorenzo et al., 2018) to the west and the Keystone thrust (99 Ma; Fleck and Carr, 1990) on the eastern edge. Near Salt Lake City, the belt widens (~500 km) and includes several thrust belts that were active for a long period of time (ca. 100 My; Herring and Green, 2016). The western edge of the belt is defined by the Luning-Fencemaker fold and thrust belt (~165-150 Ma; Wyld et al., 2003) and the eastern edge by the Hogsback thrust (~56 Ma; DeCelles, 1994).

Along strike variation in orogens are attributed to "tectonic inheritance" where the form of the orogen mirrors the form of the rifted continental margin; salients develop at the location of embayments and recesses at the location of promontories (Thomas, 1977; 2005). Variation along the Sevier orogenic belt is also suggested to be inherited from the

form of the rifted Precambrian continental margin as defined by the Cordilleran hinge

line (CHL) (Picha, 1986; Figure 1).
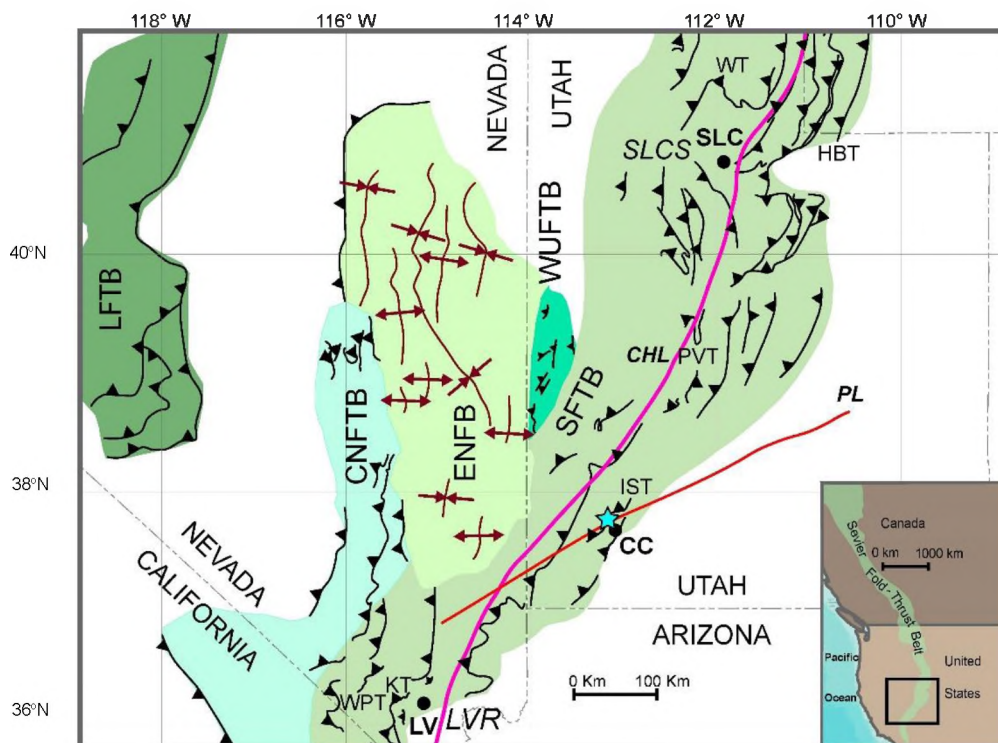
Figure 1. Location map including Sevier Orogenic deformation belts. Three Peaks marked by the blue star. LFFTB=Luning-Fencemaker Fold Thrust Belt CNFTB=Central Nevada Fold Thrust Belt; ENFB=Eastern Nevada Fold Belt; WUFTB= Western Utah Fold Thrust Belt; SFTB=Sevier Fold Thrust Belt; LV=Las Vegas; CC=Cedar City; SLC=Salt Lake City; CHL=Cordilleran hinge line; PL=Paragonah Lineament; LVR=Las Vegas Recess; SLCS=Salt Lake City Salient; KT=Keystone Thrust; WPT=Wheeler Pass Thrust; IST=Iron Springs Thrust; PVT=Pavant Thrust; PXT=Paxton Thrust; GT=GunnisonThrust; HBT=Hogsback Thrust. Compiled from Yonkee and Weil (2015), Giallorenzo et al. (2018), Willis (1999), Long (2015), Herring and Greene (2016), Picha and Gibson (1985), Stokes et al., (1963), Page et al. (2005), and Wyld et al., (2003).

Evaluating the role of tectonic inheritance and tectonic models for thrusting in the evolution of the Sevier Orogeny requires correlation of spatially distributed thrust belts in the north (e.g., Western Utah thrust belt of Greene, 2014) to the narrower zone of thrusting in the south. In the north, initiation of Sevier thrusting at ~165 Ma on the Luning-Fencemaker thrust belt was followed by rapid advancement of the front into northwestern Utah along the Canyon Range thrust at ~146 Ma, as a result of several fold and thrust belts linked to a common decollement (Herring and Greene, 2016). In contrast, the leading edge of the Sevier belt is thought to have arrived in southwest Utah at ~80 Ma on the Pavant thrust (e.g., Yonkee and Weil, 2015; Herring and Greene, 2016). Uncertainty in the timing of the eastward propagation of the leading edge along the strike of the Sevier belt precludes determining if thrusts in southwest Utah are linked to the western belts by a shared decollement (e.g., Herring and Greene, 2016) or if strain was transferred east to newly developed independent thrusts, as well as linking Sevier deformation to plate tectonic forces. We present the first complete description and high-precision zircon U-Pb geochronology of a previously unreported volcanic ash unit near the base of the synorogenic Iron Springs Formation in southwest Utah. We interpret the base of the Iron Springs Formation to include the Marshall Creek breccia, which originated as debris flows proximal to the Iron Springs thrust. Our findings place the leading edge of the Sevier orogenic belt, in the critical intervening area (~37° N), significantly further east (~50 km, e.g., see Long, 2015, fig. 6, p. 415) at an earlier point in time (100 Ma), than previously thought (Yonkee et al., 2019; Herring and Greene, 2016 fig. 2 p. 136). This age also constrains the base of the Cretaceous Iron Springs Formation as latest Albian/earliest Cenomanian.

We use these results, from the critical intervening area between Las Vegas and Salt Lake City, to evaluate the role of tectonic inheritance and magmatic flare-ups in the spatial and temporal development of the Sevier orogenic front.

2. GEOLOGY OF THREE PEAKS, IRON COUNTY, UTAH

2.1. OVERVIEW

The Three Peaks (Figure 1) form a series of rugged hills cored by Miocene quartz monzonite laccoliths (Mackin and Rowley, 1976; Barker, 1995). Cropping out on the western flank of the laccolith are the Co-op Creek Limestone and Crystal Creek Members of the Jurassic Carmel Formation (Supplementary Figure 1). These units are disconformably overlain by the synorogenic Cretaceous Marshall Creek breccia (MCb), which is in turn conformably overlain by and interfingers with synorogenic clastics of the Iron Springs Formation. Along strike to the south, the sedimentary section is folded and overturned in the footwall of the Iron Springs thrust (Mackin et al., 1976; Knudsen and Biek, 2014).

2.2. STRATIGRAPHIC RELATIONSHIPS AT THREE PEAKS

Two stratigraphic sections, the Central Creek and the Shooting Range transects, were measured at Three Peaks (Figure 2). The sections begin at the top of the shallow-marine, Co-op Creek Limestone -a light grey to blackish grey, algal-laminated, lime mudstone. The Co-op Creek Limestone is overlain by the Crystal Creek Member of the Carmel Formation. At Three Peaks, the Crystal Creek Member consists of fluvial, channelized deposits of cream white sandstons and reddish brown to maroon mudstones.
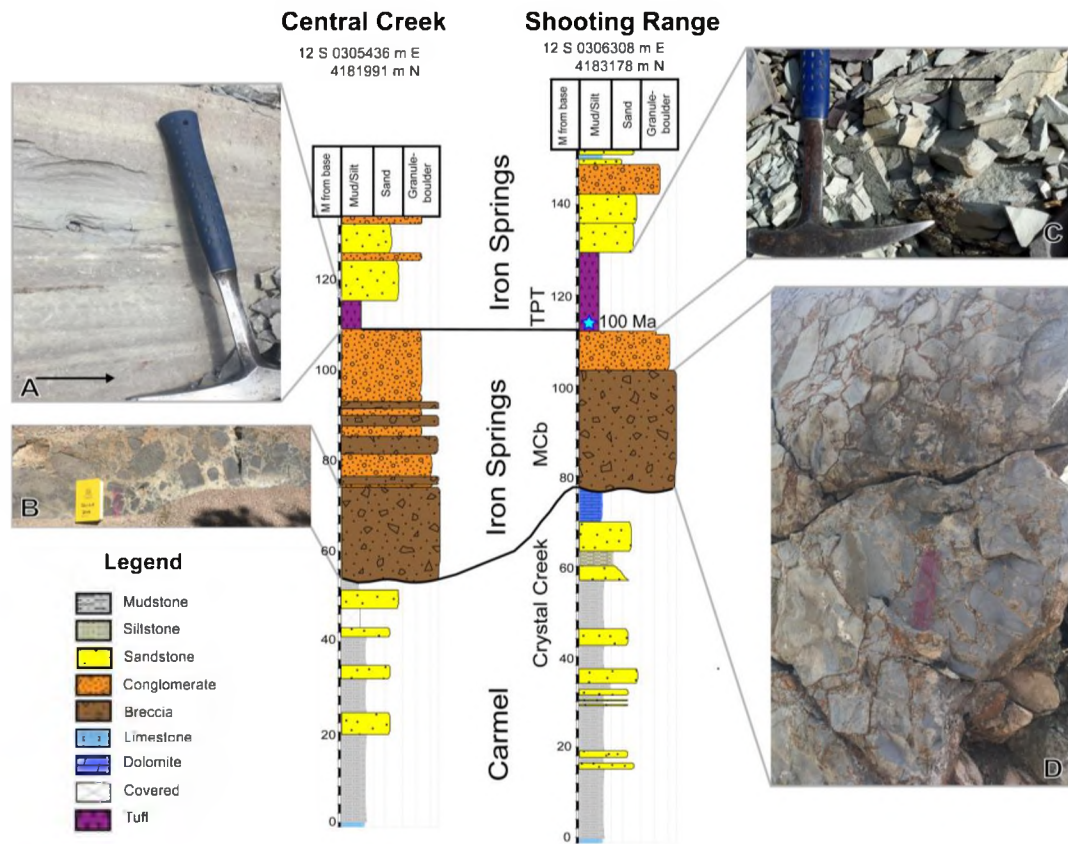
Figure 2. Stratigraphic columns. Generated using SDAR (Ortiz et al., 2013) from Three Peaks (Fig. 1). Geochronology sample of Three Peaks Tuff (TPT) marked with a blue star. Note interfingering of the Marshall Creek breccia (MCb) and the basal conglomerate of the Iron Springs Formation. A. Outcrop of the TPT, Central Creek traverse. Arrow points to accretionary lapilli. B. Outcrop of MCb, Central Creek traverse. Note the large, angular grey limestone clasts. C. Outcrop of TPT, Shooting Range traverse. Arrow points to accretionary lapilli. D. Outcrop of MCb, Shooting Range traverse. Six-inch ruler for scale.

The base of the Cretaceous is marked by the appearance of the distinctive MCb, which is confined to the Three Peaks area (Mackin, 1947) and disconformably overlies either the Crystal Creek or the Co-op Creek Members of the Carmel Formation depending on local relief on the unconformity (Figure 2).

The MCb is comprised primarily of angular, lime mudstone pebbles to boulders (>1.5 m across). Exiguous sub-to well-rounded limestone clasts were noted [supplementary figure 2]), as well as sparse well rounded quartzite pebbles and cobbles, supported by a dark brown lime-silt matrix. Limestone clasts from the MCb conspicuously resemble Co-op Creek Creek Limestone. Locally, the MCb grades upwards into, and interfingers with, a basal quartzite conglomerate of the Iron Springs Formation over a stratigraphic interval of up to ~18 m (Figure 2). Above this contact, the Iron Springs Formation consists of beds of sandstone, conglomerate, and sparse limestone beds, which locally contain intraformational rip-up clasts (Figure 2).

3. THE THREE PEAKS TUFF

We propose the name Three Peaks Tuff Member of the Iron Springs Formation, and a type section (Figure 2 Shooting Range section) for a purple to whitish grey dacite vitric-crystal coarse ash-lapilli tuff (see Schmid 1981). It is mappable along strike over several kilometers, and consists of multiple discrete beds that crop out over a stratigraphic interval of ~17 m (Figure 2). Accretionary lapilli and biotite phenocrysts are conspicuous in several beds, hand sample, and thin section (Supplementary Figure 3). Other phenocrysts include quartz, plagioclase, and iron oxides. Quartz and plagioclase phenocrysts are typically < 0.6 mm and inconspicuous in hand sample. Altered glass shards are common. Sparse lithic quartzite fragments > 0.5 mm occur near the base of the tuff and were likely locally derived during emplacement. The uppermost ash bed has been reworked, consistent with emplacement during active sediment deposition. Four

samples of the tuff, analyzed for whole rock geochemistry, plot unambiguously as

dacite with trace element signatures consistent with a volcanic arc setting (Figure 3;
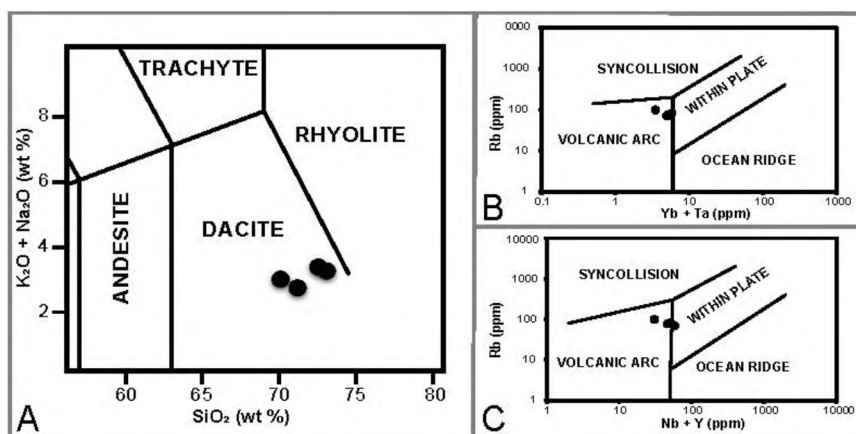
Supplementary Table 1).

Figure 3. Whole rock geochemistry. A. Total alkalis vs SiO_2 for whole rock samples of TPT. B.-C. Trace element discrimination diagrams (after Pearce, et al., 1984) for the TPT.

Geochronology: Zircons from the base of the tuff were dated by Laser Ablation

Inductively Coupled Plasma Mass Spectrometry (LA-ICP-MS) and Chemical Abrasion

Thermal Ionization Mass Spectrometry (CA-TIMS). These zircons are euhedral to

subhedral with euhedral to subhedral cores (Fig. 4). Zircons with anhedral cores are rare.

Concentric oscillatory zoning is common, though simple-, broad-, patchy-, and sector

zoning were noted. Forty-seven zircons analyzed by LA-ICP-MS yield dates between

104.7 ± 4.0 Ma and 92.6 ± 2.4 Ma (Supplementary Table 2). Thirty-nine of these

analyses have a weighted mean date of 99.4 ± 0.8 Ma (MSWD = 0.9, probability of fit =

0.57). Of these, six zircons were analyzed by CA-TIMS (Supplementary Table 3). The four youngest yield a weighted mean date of 100.18 ± 0.04 Ma (Fig. 4); the other two are slightly older (100.30 ± 0.07 Ma and 100.43 ± 0.07 Ma) and may reflect older cores. We interpret the CA-TIMS date of 100.18 ± 0.04 Ma as the crystallization age for the zircons in the Three Peaks Tuff, providing a minimum deposition age for the MCb.
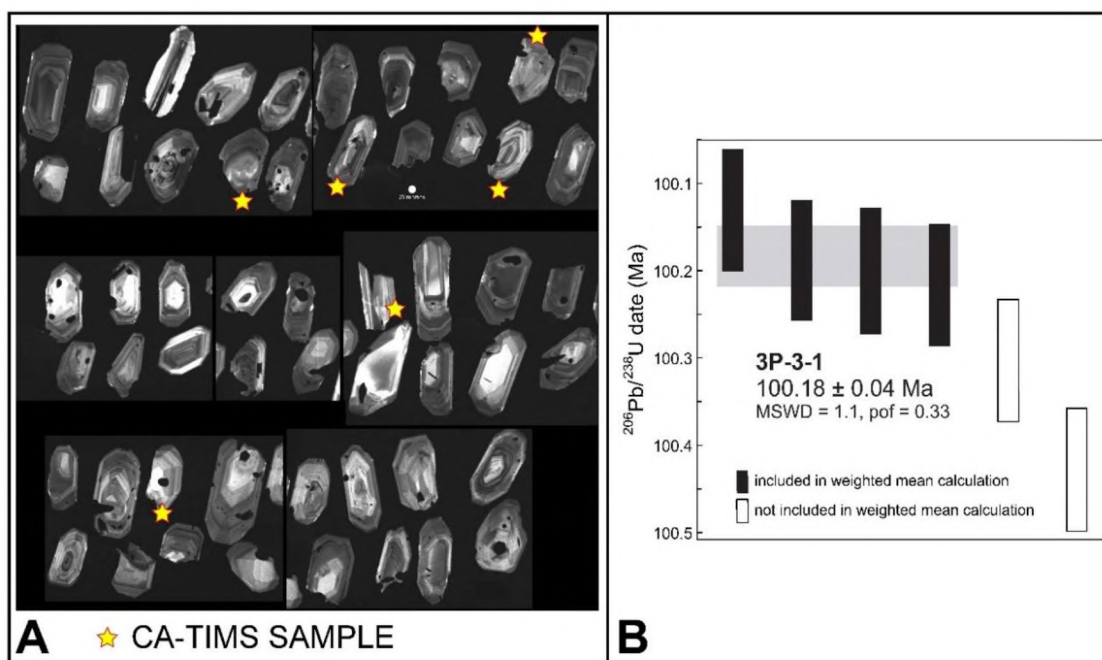

Figure 4. TPT zircons. A. Cathodoluminescence images of zircons from TPT. B. 206Pb/238U zircon dates (with error) from CA-TIMS analysis.

4. DISCUSSION

4.1. TECTONIC IMPLICATIONS OF STRATIGRAPHIC RELATIONSHIPS

Field relationships demonstrate the MCb and the Three Peaks Tuff are part of the lower Iron Springs Formation (Figure 2). The large angular clasts of the MCb originated as talus blocks transported short distances by debris flows possibly as part of a fanglomerate and alluvial fan system (e.g., Laird and Hope, 1968; Ribes et al., 2019). The Co-op Creek Limestone and limestone clasts of the MCb are visually indistinguishable (see also Mackin, 1947; Mackin and Rowley, 1976; Fillmore, 1991). We suspect that the talus was derived from the Co-op Creek Limestone as it was uplifted in the hanging wall of the emergent Iron Springs thrust at the southernmost extent of the breccia (see Mackin et al., 1976; Knudsen and Biek, 2014). Between debris flow events, sediment was supplied to the alluvial system by streams carrying quartzite and limestone eroded from bedrock uplifted by the Wah Wah Mountains thrust (Fillmore, 1991). Thus, the 100.18 ± 0.04 Ma U/Pb zircon crystallization age for the Three Peaks Tuff constrains the depositional age of the lower Iron Springs Formation and the end of the hiatus represented by the regional sub-Cretaceous unconformity to the latest Albian/earliest Cenomanian. This age also constrains the arrival of the leading edge of the SFTB in the critical intervening area between the northern and southern deformation belts. The implication of this age to understanding the evolution of the Sevier Orogeny is discussed below (Figure 1).

4.2. MAGMATISM AND GLOBAL PLATE REORGANIZATION

Orogenic events are defined by the linked processes of magmatism, metamorphism, and crustal deformation such that changes in one affects the others (e.g., DeCelles and Graham, 2015). The age and geochemical signature of the Three Peaks Tuff associate it with the North American Cordillera magmatic flare-up at 105 Ma to 90 Ma (DeCelles and Graham, 2015; Di Fiori et al., 2020). This flare-up coincides with a period of "global plate reorganization" wherein plate motions were dramatically altered worldwide, possibly due to cessation of subduction in eastern Gondwanaland after ca. 150 My of convergence (Matthews et al., 2012). We suggest this reorganization resulted in a significant increase in the rate of plate convergence along western North America, leading to the flare-up in Cordilleran arc magmatism, and widespread thrusting at ~100 Ma. Increased convergence would deliver volatiles to the mantle at an increased rate facilitating prolific production of magma (Ardila et al., 2019). This in turn resulted in an increased surface elevation of the arc, forcing the wedge taper into a supercritical condition, and, along with a higher horizontal compressive stress, resulted in rapid eastward propagation of thrusting and folding across the Sevier deformation belt (e.g., DeCelles and Graham, 2015; Lageson et al., 2001). Reasons for along strike spatial variation in deformation associated with the magmatic flare-up are discussed below.

4.3. STRUCTURAL INHERITANCE

The SFTB parallels the CHL which marks the western edge of thicker Precambrian crust least affected by rifting (Figure 1). At the latitude of Las Vegas (~36° N), the SFTB is narrower (~100 km), shorter lived (ca. 50 My), and mirrors the CHL

which is located < 20 km west of the leading-edge Sevier structures. Palinspastic

reconstruction, to account for Basin and Range extension (Wernicke et al., 1988), places

the leading-edge Sevier structures much closer to the CHL (~8 km) prior to extension.

The Las Vegas recess of the SFTB mirrors the promontory of thicker Precambrian craton

which impeded eastward thrust propagation sooner (e.g., ~99 Ma Keystone thrust) than

further to the north (Figure 1). In contrast, the Salt Lake salient of the SFTB mirrors the

presence of an embayment in the thicker Precambrian craton. Here thin-skin thrusting

was facilitated by thinner extended continental crust projecting further east into the craton

~50 km east of the CHL. At this latitude (~41° N), the SFTB remained active longer (ca.

100 My), over a wider deformation belt (~500 km), and propagated further inland (e.g.,

56 Ma Hogsback thrust, Figure 1).

5. CONCLUSIONS

The Three Peaks Tuff is a dacite ash-fall tuff that is syndepositional with the

syntectonic lowermost Iron Springs Formation which includes the syntectonic MCb at its

base. The concordant 100.18 ± 0.04 Ma U/Pb zircon crystallization age for the Three

Peaks Tuff constrains the end of the regional sub-Cretaceous hiatus, the beginning of

regional subsidence, and the emergence of the leading edge of the SFTB in southwestern

Utah to latest Albian/earliest Cenomanian. Increased subduction rates during the Mid-

Cretaceous plate reorganization event likely contributed to a ~100 Ma magmatic-flare up

and widespread shortening across the orogen. Along strike variation in the spatial and

temporal evolution of deformation associated within the Sevier orogeny is, to a large

extent, inherited from the rifted Precambrian crustal margin of western North America, including a promontory, embayment, and intervening transfer zones, leading to the Las Vegas Recess and Salt Lake Salient.

ACKNOWLEDGMENTS

REFERENCES

Ardila, A.M., Paterson, S.R., Memeti, V., Parada, M.A., and Molina, P.G., 2019, Mantle driven Cretaceous flare-ups in Cordilleran arcs: Lithos, v. 326–327, p. 19–27, https://doi: 10.1016/j.lithos.2018.12.007.

Barker, D.S., 1995, Crystallization and alteration of quartz monzonite, Iron Springs mining District, Utah: Relation to associated iron deposits: Economic Geology, v. 90, p. 2197–2217.

DeCelles, P.G., 2004, Late Jurassic to Eocene evolution of the Cordilleran thrust belt and foreland basin systems, western USA: American Journal of Science, v. 304, p. 105–168, https://doi:10.2475/ajs.304.2.105.

DeCelles, P.G., 1994, Late Cretaceous–Paleocene synorogenic sedimentation and kinematic history of the Sevier thrust belt, northeast Utah and southwest Wyoming: Geological Society of America Bulletin, v. 106, p. 32–56, https://doi:10.1130/0016-7606(1994)106<0032:LCPSSA>2.3.CO;2.

DeCelles, P.G., and Graham, S.A., 2015, Cyclical processes in the North American Cordilleran orogenic system: Geology, v. 43, p. 499–502, https://doi:10.1130/G36482.1.

Di Fiori, R.V., Long, S.P., Fetrow, A.C., Snell, K.E., Bonde, J.W., Vervoot, J, 2020, Syncontractional deposition of the Cretaceous Newark Canyon Formation, Diamond Mountains, Nevada: Implications for strain partitioning within the U.S. Cordillera: Geosphere, v. 16, p. 546–566, https://doi: 10.1130/GES02168.1.

Fillmore, R.P., 1991, Tectonic influence on sedimentation in the southern Sevier foreland, Iron Springs Formation (Upper Cretaceous), southwestern Utah, in Nations, J.D., and Eaton, J.G., eds., Stratigraphy, depositional environments; and sedimentary tectonics of the western margin, Cretaceous Western Interior Seaway: Geological Society of America Special Paper 260, p. 9-25.

Fleck, R.J., and Carr, M.D., 1990, The age of the Keystone thrust: Laser-fusion 40Ar/39Ar dating of foreland basin deposits, southern Spring Mountains, Nevada: Tectonics, v. 9, p. 467-476.

Giallorenzo, M., Wells, M.L., Yonkee, W.A., Stockli, D.F., and Wernicke, B.P., 2018, Timing of exhumation, Wheeler Pass thrust sheet, southern Nevada and California: Late Jurassic to middle Cretaceous evolution of the southern Sevier fold-thrust belt: Geological Society of America Bulletin, v. 130, p. 558–579, https://doi:10.1130/B31777.1.

Greene, D.C., 2014, The Confusion Range, west-central Utah: Fold-thrust deformation and a western Utah thrust belt in the Sevier hinterland: Geosphere, v. 10, p. 148–169, https://doi:10.1130/GES00972.1.

Herring, D. M., and Greene, D. C., 2016, The western Utah thrust belt in the larger context of the Sevier orogeny, in Comer, J.B., Inkenbrandt, P.C., Krahulec, K.A., and Pinnell, M.L., eds., Resources and Geology of Utah's West Desert: Utah Geological Association Publication 45, p. 131-146.

Knudsen, T.R., and Biek, R.F., compilers, 2014, Interim geologic map of the Cedar City NW Quadrangle, Iron County, Utah: Utah Geological Survey open file report 627, scale 1:24,000.

Lageson, D.R., Schmitt, J.G., Horton, B.K., Kalakay, T.J., and Burton, B.R., 2001, Influence of Late Cretaceous magmatism on the Sevier orogenic wedge, western Montana: Geology, 242 v. 29, no. 8, p. 723-726.

Laird, M.G., and Hope, J.M., 1968, The Torea Breccia and the Papahaua Overfold: New Zealand Journal of Geology and Geophysics, v. 11, p. 418-34. https://doi: 10.1080/00288306.1968.10423660.

Long, S.P., 2015, An upper-crustal fold province in the hinterland of the Sevier orogenic belt, eastern Nevada, U.S.A.: A Cordilleran valley and ridge in the Basin and Range: Geosphere, v. 11, p. 404–424, https://doi: 10.1130/GES01102.1.

Mackin, J.H., Nelson, W.H., and Rowley, P.D., compilers, 1976, Geologic map of the Cedar City Northwest Quadrangle, Iron County, Utah: U.S. Geological Survey, scale 1:24,000.

Mackin, J.H., and Rowley, P.D., compliers, 1976, Geologic map of the Three Peaks Quadrangle, Iron County, Utah: U.S. Geological Survey, scale 1:24,000.

Mackin, J.H., 1947, Some structural features in the intrusions in the Iron Springs district: Guidebook to the geology of Utah, no. 2: Utah Geological Society, 62 p.

Matthews, K.J., Seton, M., Muller, R.D., 2012, A global-scale plate reorganization event at 105–100 Ma: Earth and Planetary Science Letters, v. 355–356, p. 283–298, https://doi:10.1016/j.epsl.2012.08.023.

Ortiz, J., Moreno, C., Punyasena, S. W., Cardenas, A. L., and Jaramillo, C., 2013, SDAR a new quantitative toolkit for analyze stratigraphic data. Houston: NAMS-III.

Page, W.R., Lundstrom, S.C., Harris, A.G., Langenheim, V.E., Workman, J.B., Mahan, S., Paces, J.B., Dixon, G.L., Rowley, P.D., Burchfiel, B.C., Bell, J.W., and Smith, E.I., compilers, 2005, Geologic and geophysical maps of the Las Vegas 30x60 quadrangle, Clark and Nye Counties, Nevada, and Inyo County, California: U.S. Geological Survey Scientific Investigations Map 2814, scale 1: 5,000,000, 2 sheets, 58 p. text.

Pearce, J.A., Harris, N.B.W., and Tindle, A.G., 1984, Trace-element discrimination diagrams for the tectonic interpretation of granitic-rocks: Journal of Petrology, v. 25, p. 956–983.

Picha, F., 1986, The influence of preexisting tectonic trends on geometries of the Sevier orogenic belt and its foreland in Utah, in Peterson, J.A., ed., Paleotectonics and Sedimentation in the Rocky Mountain Region, United States: American Association of Petroleum Geologists, Memoir 41, p. 309–320.

Picha, F., and Gibson, R.I., 1985, Cordilleran hinge-line: Late Precambrian rifted margin of the North American craton and its impact on depositional and structural history, Utah and Nevada: Geology, v. 13 p. 465–468, https://doi:10.1130/00917613(1985)13<465:CHLPRM>2.0.CO;2.

Ribes, C., Ghienne, J.-F., Manatschal, G., Decarlis, A., Karner, G.D., Figueredo, P.H., and Johnson, C.A., 2019, Long-lived mega fault-scarps and related breccias at distal rifted margins: Insights from continental rifted margin and fossil analogues: Journal of the Geological Society [London], v. 176, no. 5, p. 801–816, https://doi: 10.1144/jgs2018-181.

Schmid, R., 1981, Descriptive nomenclature and classification of pyroclastic deposits and fragments: Recommendations of the IUGS Subcommission on the Systematics of Igneous Rocks: Geology, v. 9, p. 41-43.

Stokes, W.L., Madsen, J.H., Hintze, L.F., compilers, 1963, Geologic Map of Utah, Utah State Land Board, scale 1:250000.

Thomas, W.A., 2005, Tectonic inheritance at a continental margin: GSA Today, v. 16, no. 2, p. 4-11, https://doi: 10.1130/1052-5173(2006)016[4:TIAACM]2.0.CO;2.

Thomas, W.A., 1977, Evolution of Appalachian-Ouachita salients and recesses from reentrants and promontories in the continental margin: American Journal of Science, v. 277, p. 1233–1278.

Wernicke, B., Axen, G.J., and Snow, J.K., 1988, Basin and Range extensional tectonics at the latitude of Las Vegas, Nevada: Geological Society of America Bulletin, v. 100, p. 1738-1757.

Willis, G.C., 1999, The Utah Thrust System – An Overview, in Spangler, L.W., and Allen, C.J., eds., Geology of northern Utah and vicinity: Utah Geological Association Publication 27, p. 1-9.

Wyld, S.J., Rogers, J.W., and Copeland, P., 2003, Metamorphic evolution of the Luning-Fencemaker fold-thrust belt, Nevada: Illite crystallinity, metamorphic petrology, and 40Ar/39Ar geochronology: The Journal of Geology, v. 111, p. 17–38, https://doi:10.1086/344663.

Yonkee, W.A., Eleogram, B., Wells, M.L., Stockli, D.F., Kelley, S., and Barber, D.E., 2019, Fault slip and exhumation history of the Willard Thrust Sheet, Sevier Fold-Thrust Belt, Utah: Relations to wedge propagation, hinterland uplift, and foreland basin sedimentation: Tectonics, v. 38, p. 2850-2893, https://doi:10.1029/2018TC005444.

Yonkee, A., and Weil, A.B., 2015, Tectonic evolution of the Sevier and Laramide belts within the North American Cordillera orogenic system: Earth-Science Reviews, v. 150, p. 531–593, https://doi: 10.1016/j.earscirev.2015.08.001.

SECTION

2. CONCLUSIONS

The Three Peaks Tuff was emplaced soon after the deposition of the lowermost synorogenic Iron Springs Formation, which records initial movement on the Iron Springs thrust. Therefore, the 100.18 Ma date obtained from zircons in the Three Peaks Tuff provides valuble thrust kinematic data for the Iron Springs thrust. Due to the strong temporal linking of Sevier thrusting at 100 Ma with a marked increase in magma production, as well as with the global mid-Cretaceous plate reorganization event, it is suggested that increased convergence rates related to this event drove both magma production and thrust propagation. Additionally, the Paragonah Lineament and the Cordillerian Hingeline were critical controls on the evolution of the Sevier Fold and Thrust Belt.

APPENDIX A.

SUPPLEMENTAL FILE SUBMITTED WITH PAPER I

1. INDEX TO SUPPLEMENTARY MATERIAL

Figure A.1. Geologic map of the Three Peaks area. Compiled from Mackin and Rowley (1976) and Mackin et al. (1976).

2. FIELD AND PETROGRAPHIC DESCRIPTION OF THE THREE PEAKS TUFF

The Three Peaks Tuff is a primary vitric-crystal coarse ash-lapilli and secondary (reworked) tuff consisting of multiple beds, outcropping over a stratigraphic interval of about 18 m. It is traceable along strike across the margin of Three Peaks from the Northwest Intrusive Fault of Mackin and Rowley (1976), to the south where it is again truncated by normal faulting. The tuff varies in color from deep purple to cream white (Figure A.2).

Figure A.2. An outcrop of the Three Peaks Tuff showing some of the color variability. Note both the purple and white beds. 35L pack for scale.

Accretionary lapilli and biotite phenocrysts are conspicuous in hand sample and outcrop. In thin section, altered glass fragments, quartz, and plagioclase phenocrysts may be seen, even though overall crystallinity is low (~5%-20%) (Figures A.3; A.4). Grains tend to be angular and have a shattered appearance, except in the uppermost bed where grains are rounded due to secondary reworking (Figure A.5). In samples lacking evidence of reworking, grains are typically preferentially aligned, with the long axes perpendicular to bedding (Figure A.6).
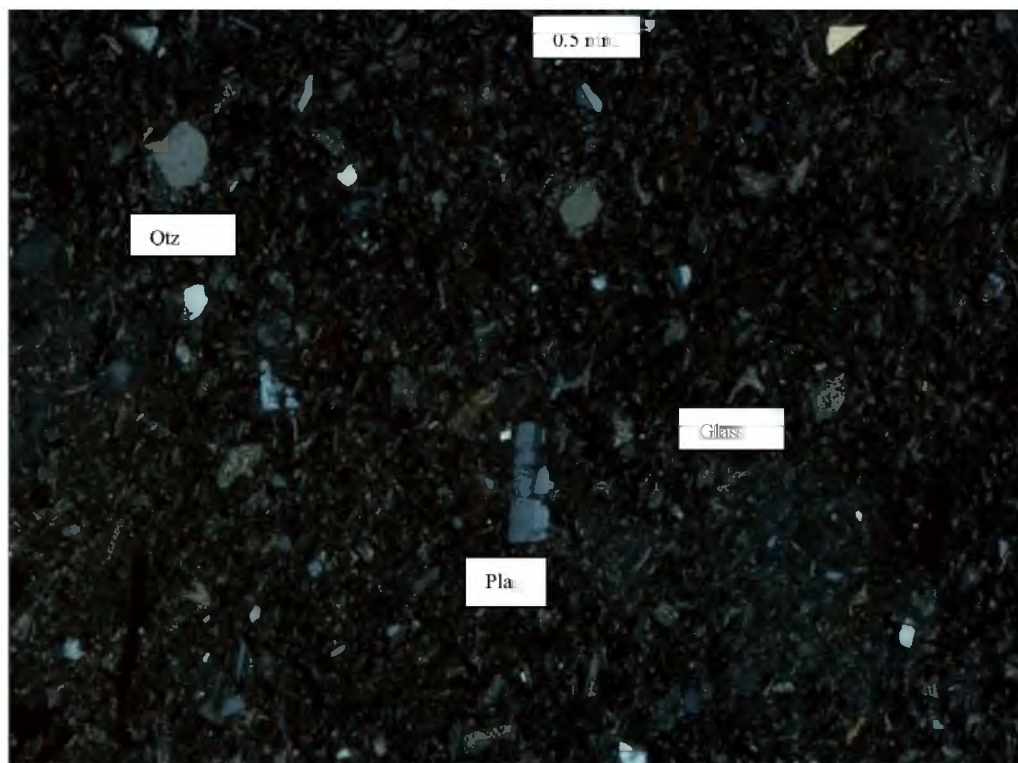
Figure A.3. Shows altered glass as well as small plagioclase and quartz grains.
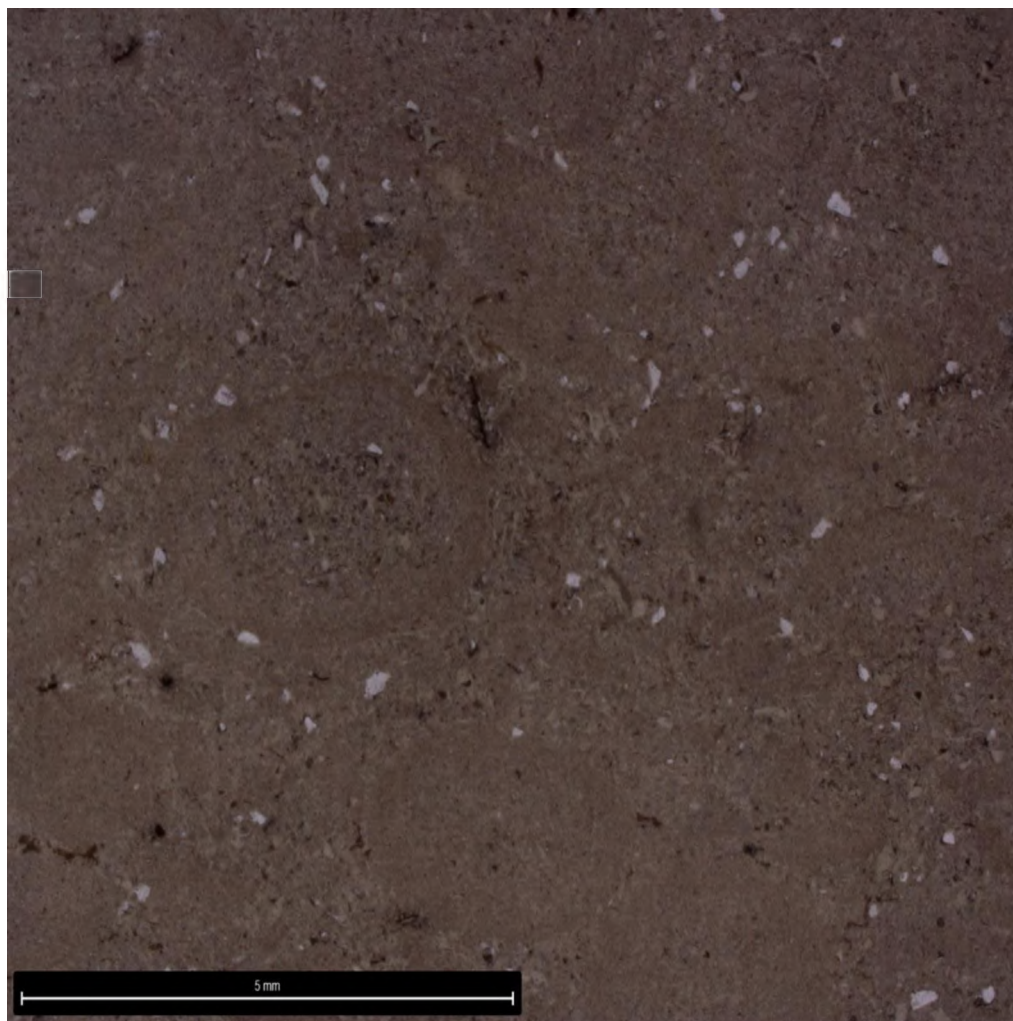
Figure A.4. Reflected light image showing accretionary lapilli. Scale bar is 5 mm long.
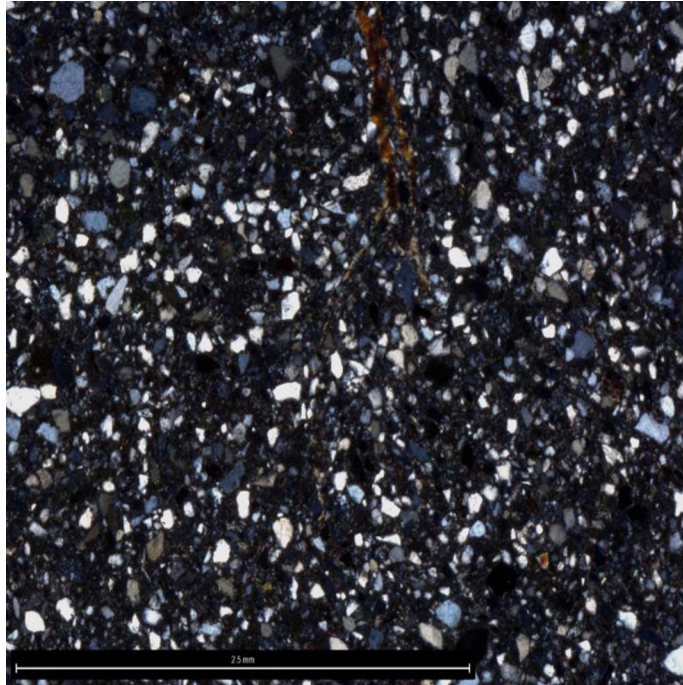
Figure A.5. Shows rounded, reworked grains from the topmost bed of the Three Peaks Tuff. Scale bar is 2.5 mm.
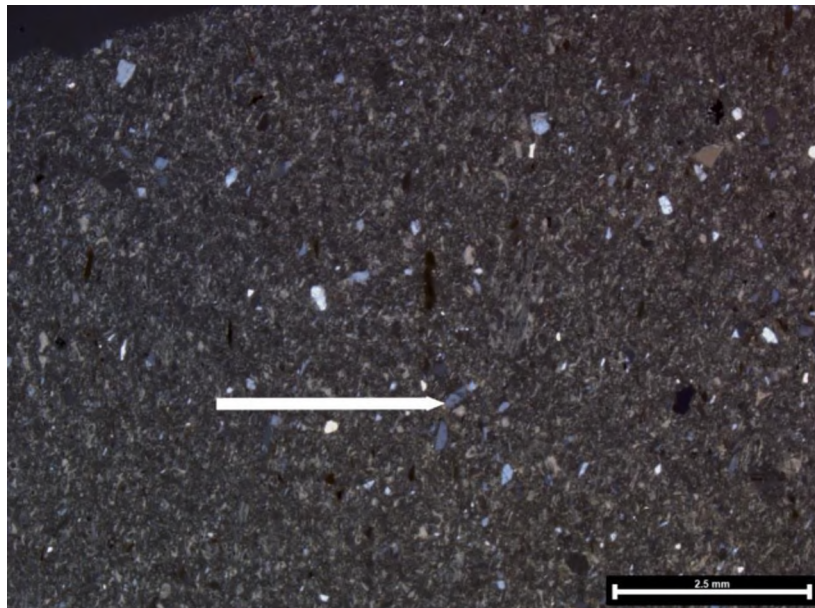
Figure A.6. Shows grains aligned perpendicular to bedding direction (represented by the white arrow). Note the relatively large biotite grains.

Especially near the base of the tuff, sparse quartzite lithics, significantly larger than surrounding grains are found (Figure A.7).
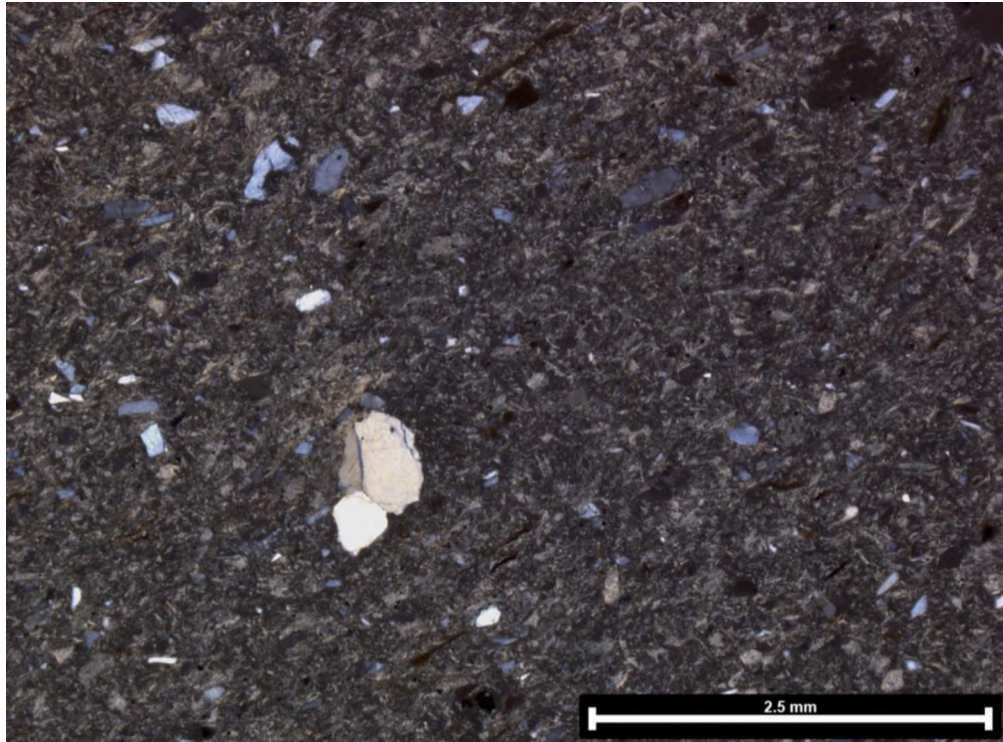
Figure A.7. Quartzite lithic fragment in Three Peaks Tuff. Note the triple junction.

Little alteration is evident in outcrop, except near the fault truncation to the south, where it is disturbed by faulting, and where iron-rich fluids have exploited nearby normal faults (Figures A.8; A.9).

Figure A.8. Three Peaks Tuff (purple) near the southern fault truncation.

Figure A.9. Three Peaks Tuff (white) near the southern fault truncation.

We interpret the Three Peaks Tuff to be an ash fall tuff deposited during active orogenic sedimentation. The presence of accretionary lapilli, the size and distribution of phenocrysts, as well as the presence of altered glass are consistent with emplacement by ash fall. Quartzite xenoliths were likely derived from the underlying quartzite conglomerate of the Iron Springs Formation. Reworking of the uppermost tuff bed is also consistent with emplacement of the tuff during active deposition of the other members of the Iron Springs Formation. For more detailed thin section descriptions and microphotographs of the Three Peaks Tuff please see the proceeding section (p. 19).

Table A.1. Samples collected.

Sample	Purpose	Zone	Easting	Northing	Field Description	Actions ken
3PT-01	petrography/geochem	12S	305100	4181828	Purplish grey groundmass. 7%-10% crystalinity. Dominant phenocryst phase is biotite. Phenocrysts rangein size from 1-1.5mm	Thin section made, whole rock geochemical analysis
3PT-06	petrography/geochem	12S	305100	4181828	(bottom of the volcanics) White groundmass. Some crystals too small to be identified with a hand lens noted. Biotite? They "glint" in the sun.	Thin section made
6-16-02	petrography/geochem	12S	306210	4183290	(Bottom of another strat traverse of the volcanics) Purple groundmass. Minor biotite flakes. A few feldspars?	Thin section made
6-16-04	petrography/geochem	12S	306211	4183298	Purple groundmass. Minor feldspars and micas noted.	Thin section made, whole rock geochemical analysis
6-16-06	petrography/geochem	12S	306219	4183300	Deep purple groundmass. Apprx. 5% micas. Less than 1% plag.	Thin section made
6-16-07	petrography/geochem	12S	306222	4183297	Whitish gray green groundmass. Apprx 5% of the modal comp is small, as yet unidentified black minerals. 1% micas. GPS is at lower contact.	Thin section made
6-16-09	petrography/geochem	12S	306225	4183302	(Top of another strat traverse of the volcanics.) Light greenish grey groundmass. Very small mica and quartz crystals noted, which together comprise less than 1% of the modal comp.	Thin section made
6-16-10	petrography/geochem	12S	305460	4182016	Black to light grey Dunham mudstone (Homestake mbr, Carmel fm). Sample taken from the top of the mbr.	Thin section made
6-21-01	Petrography	12S	305059	4181828	Limestone conglomerate with rounded to angular clasts. Pebble to cobble size. Supported by a blackish grey sandy lime matrix.	Thin section made
6-21-03	Petrography	12S	305022	4181832	Blackish blue coarse grained sandstone with floating limestone pebbles near the top.	Thin section made
6-25-03	Petrography	12S	306170	4183315	Rounded to angular limestone clasts in a grey sandy lime matrix. Located on the shooting range strat column.	Thin section made
6-29-04	petrography/geochem	12S	305086	4181826	Apprx 12-18 cm thick/ White groundmass. 99% or greater groundmass	Thin section made, whole rock geochemical analysis
6-29-05	petrography/geochem	12S	305074	4181828	Greenish tan groundmass.Minor white lapilli and minor mafics. 98%-99% groundmass	Thin section made
3P-3-1	petrography/geochem/geochron	12S	306221	4183214	Collected at the base of the ash	Thin section made, zircons extracted, analyized, whole rock geochemistry analysis

Table A.2. Total alkali silicate whole rock data from the Three Peaks Tuff.

Sample no.	3P-3-1*	3PT-1*	6-29-04*	6-16-04*	Repeat 3PT-1	Repeat 6-16-04
(wt. %) SiO_2	73.09	71.19	70.09	72.55	70.95	72.11
(wt. %) Na_2O	1.62	0.98	1.68	1.68	1.01	1.67
(wt. %) K_2O	1.46	1.58	1.14	1.52	1.57	1.52

*This value used in the TAS diagram (Figure 3 main text)

Table A.3. Selected whole rock trace element data from the Three Peaks Tuff.

Sample no.	3P-3-1*	3PT-01*	6-29-04*	6-16-04*	Repeat 6-16-04	Repeat 6-16-04
Rb (ppm)	76.5	98.6	69.4	81.5	81.9	81.2
Ta (ppm)	1.2	1.2	1.3	1.2	1.1	1.2
Nb (ppm)	11	12	21	11	9	11
Yb (ppm)	4.1	2.3	3.7	4.6	4.1	4.2
Y (ppm)	35.9	18.7	37	39.6	39.5	40.4

*This value used in constructing discrimination diagrams (Figure 3 main text)

Table A.4. CA-TIMS Zircon Data from the Three Peaks Tuff.

								Radiogenic Isotope Ratios							
Sample (a)	LA-ICPMS spot label	$\frac{Th}{U}$ (b)	$^{206}Pb^*$ x10^{-13} mol (c)	mol % $^{206}Pb^*$ (c)	$\frac{Pb^*}{Pb_c}$ (c)	Pb_c (pg) (c)	$\frac{^{206}Pb}{^{204}Pb}$ (d)	$\frac{^{208}Pb}{^{206}Pb}$ (e)	$\frac{^{207}Pb}{^{206}Pb}$ (e)	% err (f)	$\frac{^{207}Pb}{^{235}U}$ (e)	% err (f)	$\frac{^{206}Pb}{^{238}U}$ (e)	% err (f)	corr. coef.
3P-3-1															
z3	264	0.414	2.4686	99.88%	239	0.25	14718	0.132	0.048101	0.079	0.104085	0.140	0.015701	0.070	0.935
z6	283	0.509	1.7208	99.89%	283	0.15	17003	0.163	0.048095	0.086	0.103941	0.146	0.015681	0.071	0.923
z4	265	0.428	2.5344	99.90%	304	0.20	18637	0.137	0.048118	0.072	0.103899	0.136	0.015667	0.070	0.958
z5	272	0.448	0.5140	99.74%	112	0.11	6840	0.143	0.048079	0.168	0.103799	0.220	0.015665	0.073	0.803
z2	260	0.455	2.1185	99.93%	398	0.13	24256	0.145	0.048086	0.079	0.103801	0.139	0.015663	0.070	0.935
z1	259	0.383	1.7717	99.77%	125	0.34	7768	0.122	0.048088	0.101	0.103744	0.158	0.015654	0.071	0.894

Table A.5. Ca-TIMS Results from the Three Peaks Tuff.

	Isotopic Dates						include in weighted mean?	Weighted Mean Calculations			
Sample (a)	$\frac{^{207}Pb}{^{206}Pb}$ (g)	± (f)	$\frac{^{207}Pb}{^{235}U}$ (g)	± (f)	$\frac{^{206}Pb}{^{238}U}$ (g)	± (f)					
z3	103.20	1.86	100.54	0.13	100.43	0.07		206Pb/238U ± random (+tracer) [+decay constant]	MSWD =	1.1	
								± 0.04 (0.06)			
z6	102.89	2.04	100.41	0.14	100.30	0.07		100.18 [0.12]	pof =	0.33	
z4	104.00	1.71	100.37	0.13	100.22	0.07	x		n =	4	
z5	102.11	3.98	100.28	0.21	100.20	0.07	x				
z2	102.43	1.86	100.28	0.13	100.19	0.07	x				
z1	102.53	2.39	100.23	0.15	100.13	0.07	x				

Table A.6. LA-ICP-MS data and results.

CA-TIMS label	207Pb*/235U*	±2σ (%)	206Pb*/238U	±2σ (%)	error corr.	207Pb*/206Pb*	±2σ (%)	207Pb*/206Pb* (Ma)	±2σ (Ma)	207Pb*/235U (Ma)	±2σ (Ma)	206Pb*/238U* (Ma)	±2σ (Ma)	% disc.
	0.10249	6.80	0.01637	3.82	0.55	0.04540	5.63	-34	137	99	6	104.7	4.0	408
	0.10003	10.45	0.01636	3.73	0.35	0.04435	9.77	-91	240	97	10	104.6	3.9	215
z2	0.10815	9.31	0.01622	3.25	0.34	0.04837	8.72	117	206	104	9	103.7	3.3	12
	0.11570	11.83	0.01600	4.09	0.34	0.05243	11.09	304	253	111	12	**102.4**	**4.2**	66
	0.10449	10.96	0.01597	3.88	0.35	0.04746	10.25	73	244	101	11	**102.1**	**3.9**	-41
	0.09922	9.90	0.01590	3.20	0.32	0.04525	9.36	-42	228	96	9	**101.7**	**3.2**	341
	0.11157	10.86	0.01586	4.99	0.45	0.05101	9.65	241	222	107	11	**101.5**	**5.0**	58
z3	0.10539	8.66	0.01584	3.32	0.37	0.04827	8.00	113	189	102	8	**101.3**	**3.3**	10
	0.09849	9.55	0.01582	2.85	0.29	0.04516	9.11	-47	222	95	9	**101.2**	**2.9**	315
	0.12161	5.88	0.01582	2.62	0.43	0.05576	5.27	443	117	117	6	**101.2**	**2.6**	77
	0.10254	10.09	0.01579	4.10	0.40	0.04709	9.22	54	220	99	10	**101.0**	**4.1**	-87
	0.10741	6.21	0.01579	2.52	0.39	0.04934	5.68	164	133	104	6	**101.0**	**2.5**	38
	0.10990	5.28	0.01573	3.59	0.67	0.05068	3.86	226	89	106	5	**100.6**	**3.6**	56
z5	0.08843	19.75	0.01570	3.91	0.19	0.04086	19.36	-296	494	86	16	**100.4**	**3.9**	134
	0.10576	7.04	0.01569	3.19	0.44	0.04889	6.27	142	147	102	7	**100.4**	**3.2**	30
	0.09618	10.11	0.01569	3.74	0.36	0.04447	9.39	-85	230	93	9	**100.3**	**3.7**	219
	0.09943	3.95	0.01567	2.66	0.65	0.04601	2.92	-2	70	96	4	**100.3**	**2.6**	5549
z6	0.10799	9.28	0.01567	3.88	0.41	0.04998	8.43	194	196	104	9	**100.2**	**3.9**	48
z1	0.09582	10.22	0.01567	2.38	0.22	0.04436	9.94	-91	244	93	9	**100.2**	**2.4**	210
	0.10955	8.58	0.01565	2.92	0.33	0.05078	8.07	231	186	106	9	**100.1**	**2.9**	57
	0.10113	9.15	0.01563	3.31	0.35	0.04693	8.53	46	204	98	9	**100.0**	**3.3**	-119
	0.10249	7.54	0.01559	3.15	0.41	0.04767	6.86	83	163	99	7	**99.7**	**3.1**	-20
	0.10060	12.95	0.01558	4.60	0.35	0.04684	12.10	41	289	97	12	**99.6**	**4.6**	-142
	0.11125	7.97	0.01556	3.59	0.44	0.05184	7.12	279	163	107	8	**99.6**	**3.5**	64
	0.09844	9.75	0.01556	3.22	0.32	0.04588	9.20	-9	222	95	9	**99.5**	**3.2**	1261
	0.09265	12.36	0.01556	4.31	0.34	0.04319	11.59	-156	288	90	11	**99.5**	**4.3**	164
	0.10362	13.39	0.01547	5.08	0.38	0.04856	12.39	127	292	100	13	**99.0**	**5.0**	22
	0.11048	11.36	0.01547	3.30	0.28	0.05180	10.86	276	249	106	11	**99.0**	**3.2**	64
	0.10252	6.41	0.01547	3.16	0.48	0.04806	5.57	102	132	99	6	**99.0**	**3.1**	3
	0.10361	7.71	0.01547	2.35	0.29	0.04858	7.35	128	173	100	7	**99.0**	**2.3**	22
	0.10232	6.33	0.01541	2.82	0.43	0.04815	5.66	107	134	99	6	**98.6**	**2.8**	7
	0.10362	5.67	0.01541	3.30	0.57	0.04877	4.61	137	108	100	5	**98.6**	**3.2**	28
	0.09133	10.82	0.01540	4.16	0.38	0.04301	9.99	-167	249	89	9	**98.5**	**4.1**	159
	0.10350	5.32	0.01536	2.85	0.52	0.04887	4.49	142	105	100	5	**98.3**	**2.8**	31
	0.09502	10.51	0.01535	3.45	0.32	0.04491	9.92	-61	242	92	9	**98.2**	**3.4**	262
	0.10021	10.00	0.01531	2.74	0.27	0.04747	9.62	73	229	97	9	**98.0**	**2.7**	-35
	0.09936	7.68	0.01530	2.83	0.36	0.04711	7.14	55	170	96	7	**97.9**	**2.7**	-79
z4	0.10617	8.01	0.01529	3.57	0.44	0.05036	7.17	212	166	102	8	**97.8**	**3.5**	54
	0.09937	5.25	0.01516	2.60	0.48	0.04755	4.57	77	108	96	5	**97.0**	**2.5**	-26
	0.11126	10.31	0.01515	3.44	0.33	0.05326	9.72	340	220	107	10	**96.9**	**3.3**	71
	0.09730	9.35	0.01513	3.05	0.32	0.04662	8.83	30	212	94	8	**96.8**	**2.9**	-222
	0.10460	8.15	0.01510	2.63	0.31	0.05024	7.71	206	179	101	8	**96.6**	**2.5**	53
	0.12210	10.16	0.01504	3.64	0.35	0.05889	9.49	563	207	117	11	**96.2**	**3.5**	83
	0.10209	5.66	0.01491	1.39	0.22	0.04966	5.48	179	128	99	5	**95.4**	**1.3**	47
	0.09264	15.84	0.01483	4.73	0.30	0.04530	15.12	-40	367	90	14	**94.9**	**4.5**	340
	0.10606	10.34	0.01460	3.95	0.38	0.05270	9.56	316	217	102	10	**93.4**	**3.7**	70
	0.11055	12.83	0.01447	2.65	0.20	0.05541	12.55	429	280	106	13	**92.6**	**2.4**	78

Weighted mean age (bold values)= 99.4+/-0.8 Ma

Figure A.10. An outcrop of the matrix supported Marshall Creek breccia along the Central Creek traverse. Note that while most of the grey limestone clasts are distinctly angular, occasional clasts are sub-rounded. Field notebook for scale.

Figure A.11. An outcrop of Marshall Creek breccia containing the rounded quartzite clasts characteristic of the basal Iron Springs Formation.

Figure A.12. Conglomerate bed in the Iron Springs Formation containing well-rounded quartzite and grey limestone clasts.

Figure A.13. Outcrop of the Three Peaks Tuff along the Central Creek transect. Yellow arrow points to accretionary lapilli. Rock hammer for scale.

3. THIN SECTION DESCRIPTIONS

3.1. SEDIMENTARY ROCKS

3.1.1. Sample 6-16-10. This is a sample of the Co-op Creek Limestone. It is a dark grey, fine-grained limestone. Some small, (silt and smaller) rare quartz grains are present, but observable only in thin section.
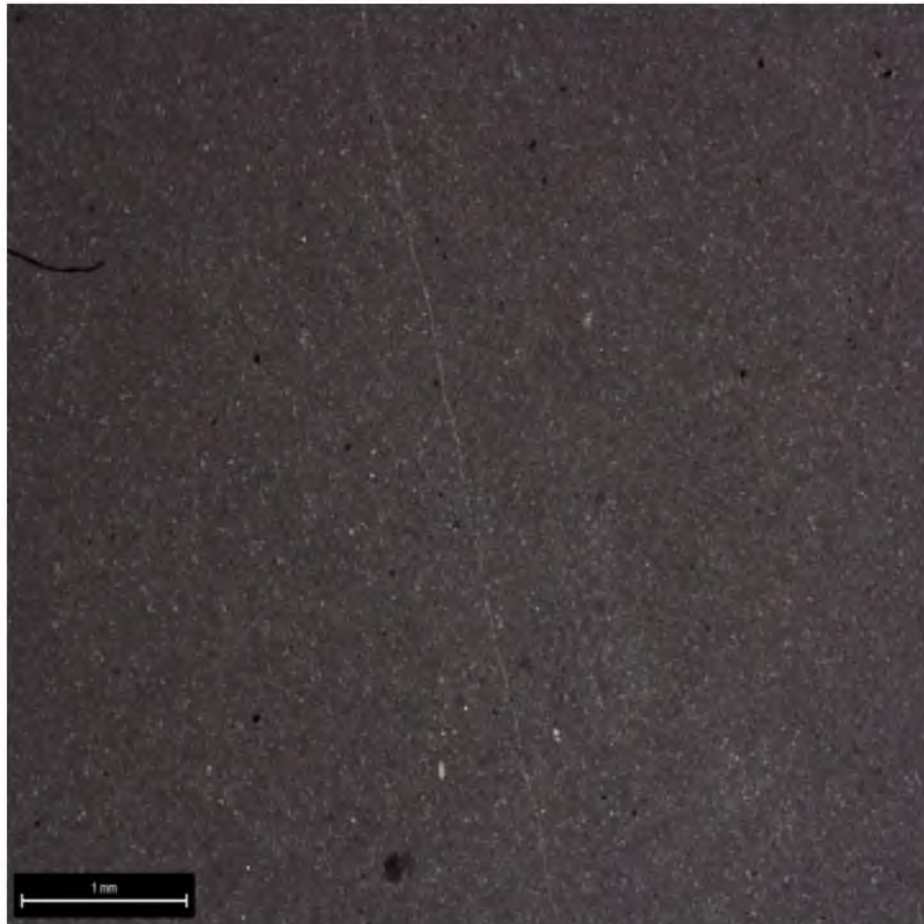

Figure A.14. Shows the character of the Co-op Creek sample in thin section. Cross polarized light.

3.1.2. Sample 6-21-03. This is part of the Iron Springs Formation, just a few meters above the Three Peaks Tuff along the Central Creek transect. The sample is a coarse-grained quartz sandstone with occasional quartzite, limestone, pebble-sized clasts. Sand grains range in shape from well rounded to angular. It is grain supported with a calcite cement.
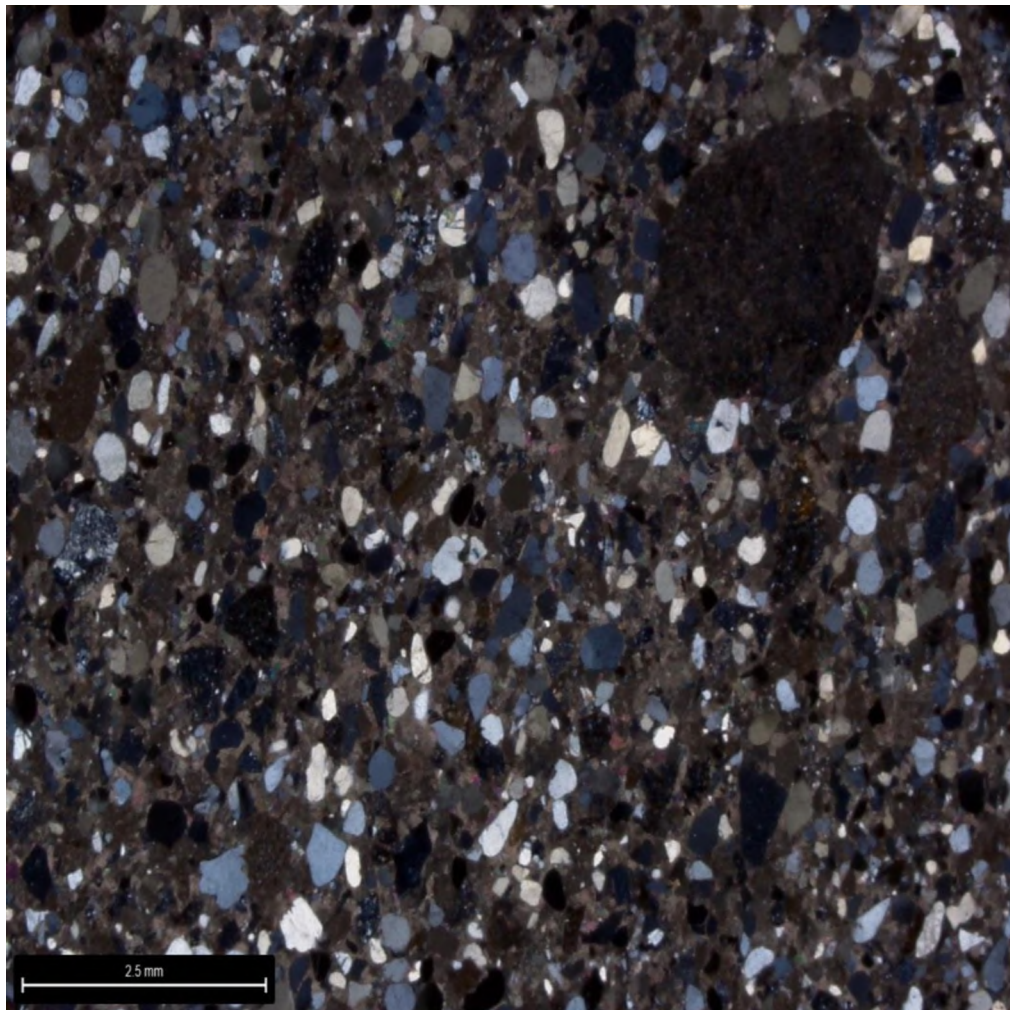

Figure A.15. Image in cross polarized light showing the quartz-rich sandstone. Note the subrounded limestone clast in the upper right hand corner.

3.1.3. Sample 6-22-01. This sample is part of the Iron Springs Formation, and was taken directly overlying the Three Peaks Tuff. It contains pebble to cobble-sized "splotchy" limestone clasts (observable in hand sample) set in a sandy-lime matrix. Splotchy limestone clasts are interpreted to be subaqueous rip-up clasts, and may be related to seismic activity on the nearby Iron Springs Thrust. From the Central Creek transect.
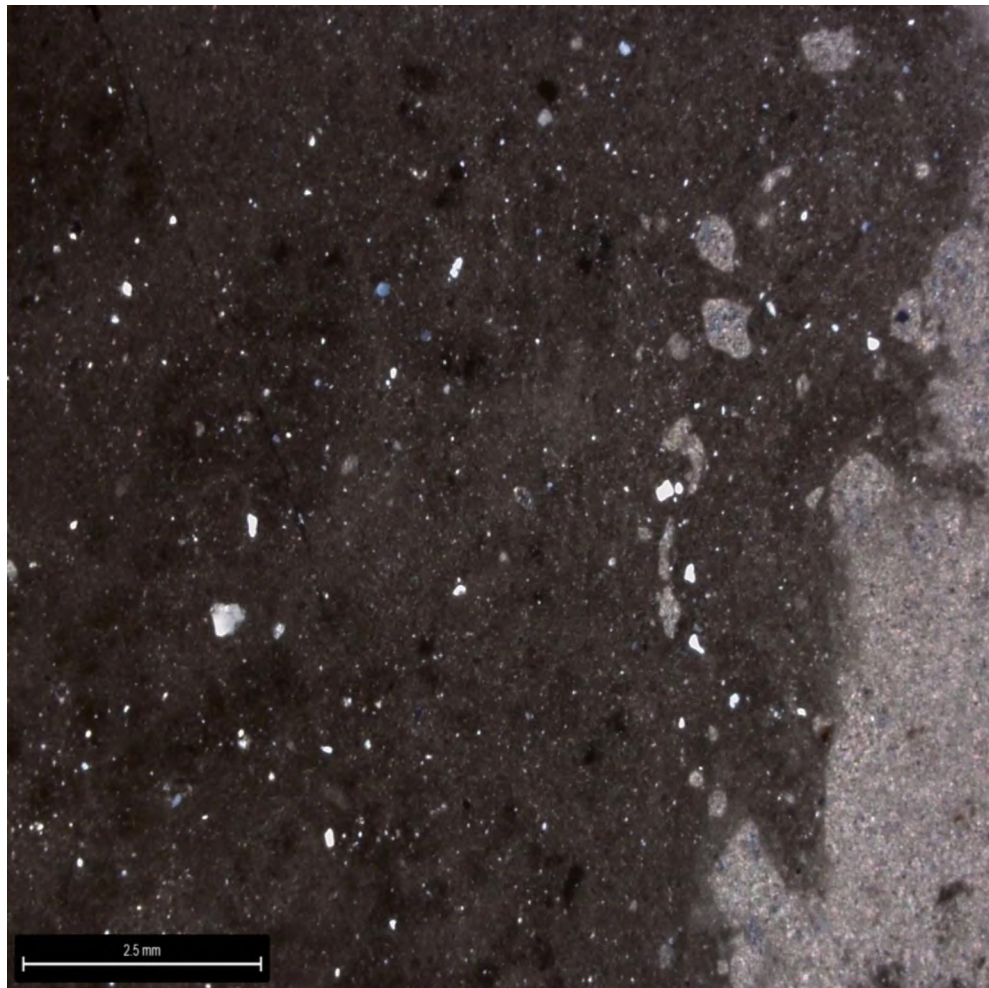

Figure A.16. Thin section image of 6-22-01 in cross polarized light.

3.1.4. Sample 6-25-03. This sample of the Iron Springs Formation was taken on the Shooting Range traverse above the Three Peaks Tuff. It contains rounded to angular limestone clasts floating in a grey, fine sandy matrix. Sand grains are predominately quartz with minor feldspar, and appear to be at least partially supported by a lime mud matrix. Grains range in shape from well rounded to angular.
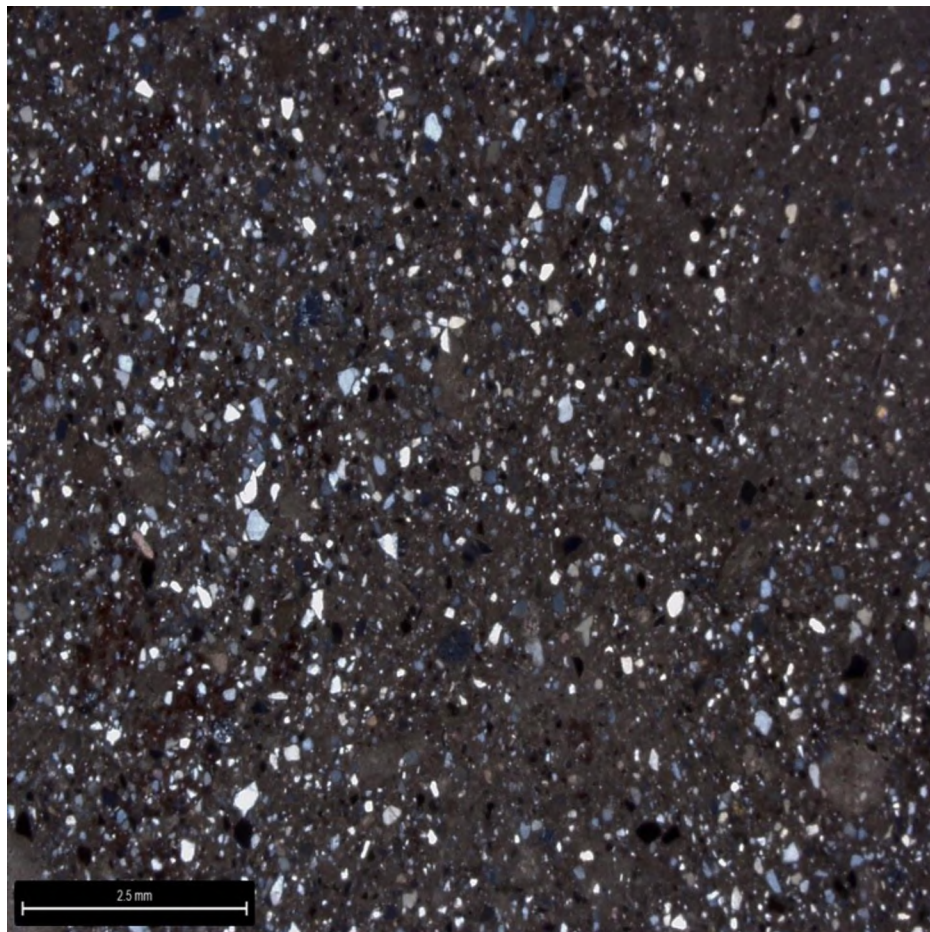

Figure A.17. Image of sample 6-25-03 in cross polarized light.

3.2. THE THREE PEAKS TUFF

3.2.1. Sample 3P-3-1. Sample taken from the base of the tuff near the Shooting Range Transect.

3.2.1.1. Phases. Phenocrysts appear to make up less than 5% of the modal composition, and consist primarily of quartz, plagioclaise, iron oxides, and biotite. Biotite grains tend to be the largest phases, though all phenocryst phases rarely exceed 0.6mm along any axis. Plagioclase is twinned, and occasionally displays what may be sieved texturing. Quartz and plagioclase phenocrysts are approximately the same size.

3.2.1.2. Textures. All phenocrysts exhibit a shattered and angular appearance. Devitrified glass is also present. Lapilli are not apparent in this sample like they are in 6-16-04. Long axes of minerals are aligned perpendicular to the "up" direction, similar to 6-16-04. Quartzite lithics may be seen in both hand sample and thin section, and are typically much larger than the surrounding phenocrysts. A cluster of anomalously rounded quartz grains was also noted (Figure. A.18). Biotite was likely the first phase to crystalize from the magma chamber, followed by plagioclase, Iron oxides, and quartz. The quartzite conglomerates of the Iron Springs Formation, which both underlies and overlies the Tuff at Three Peaks is the most likely source for the quartzite lithics, as well as the anomalously rounded quartz grains, as it seems unlikely, given the relative size of the lithics, that they were derived from rocks adjacent to the caldera and transported by wind to Three Peaks.
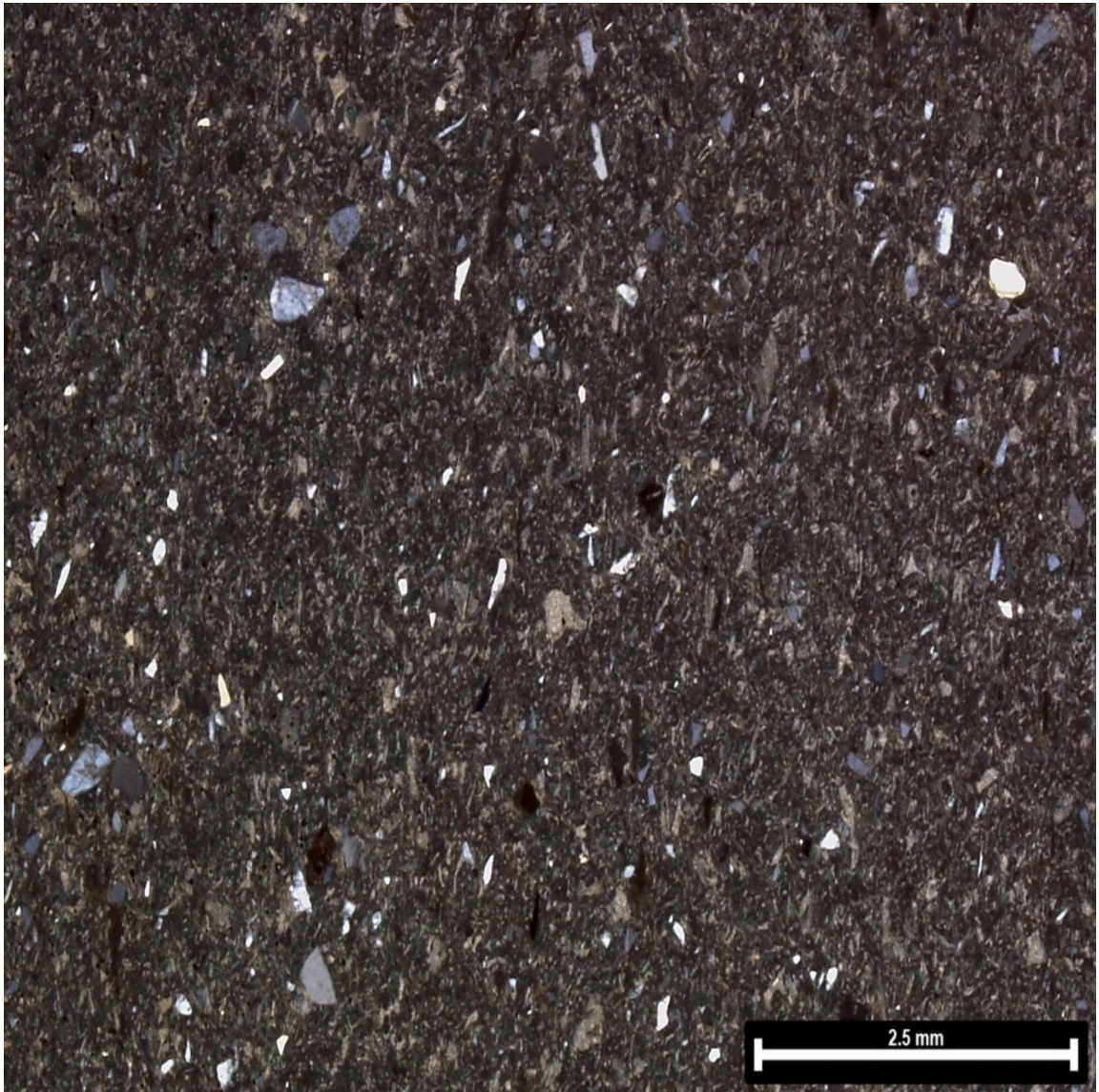
Figure A.18. Shows the general texture and composition of the sample in cross polarized light.
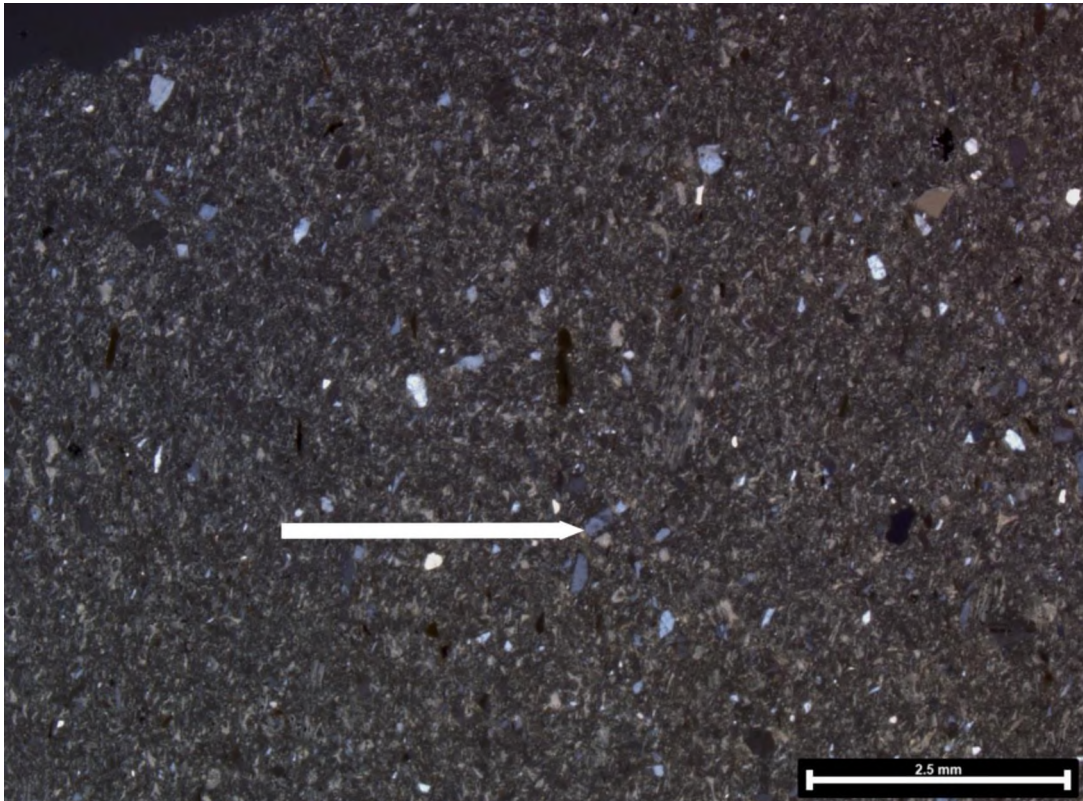
Figure A.19. 3P-3-1 White arrow shows the "up" direction. There is an alignment of minerals along their long axis perpendicular to "up." Biotite is relatively abundant in this sample.
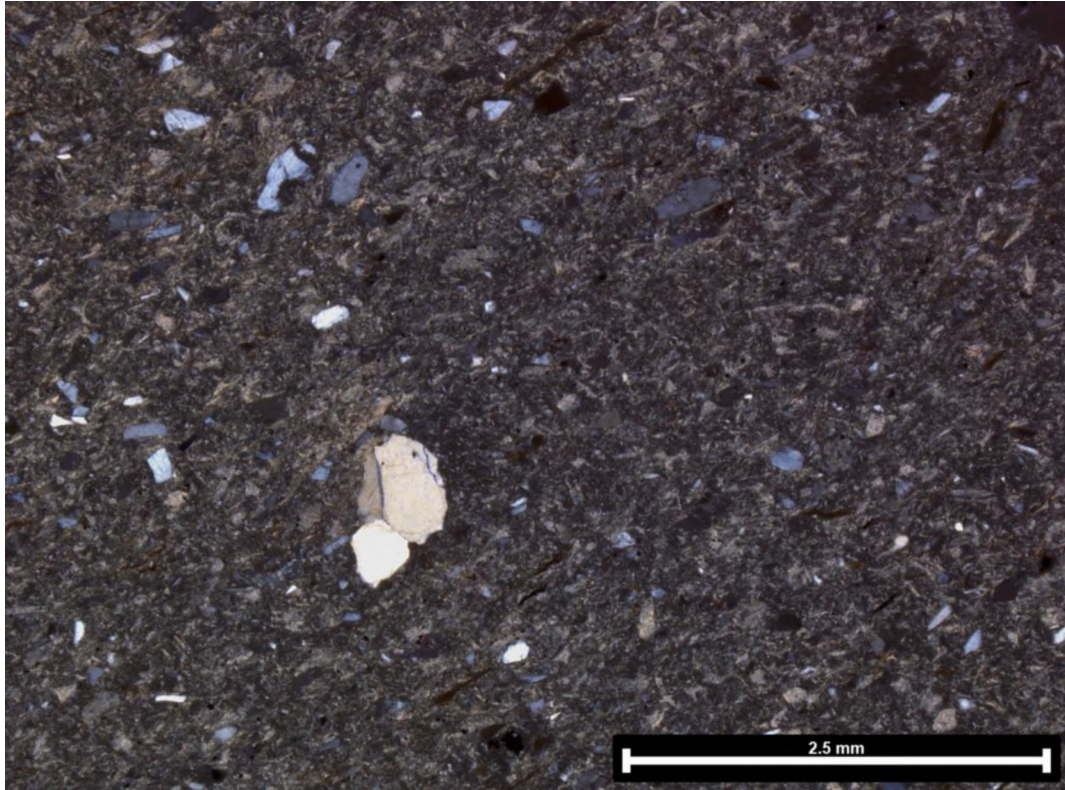
Figure A.20. Quartzite lithic fragment. Note the triple junction. Likely derived from the encasing Iron Springs Formation. Other rare quartzite lithic fragments are observed in hand specimen of this sample.
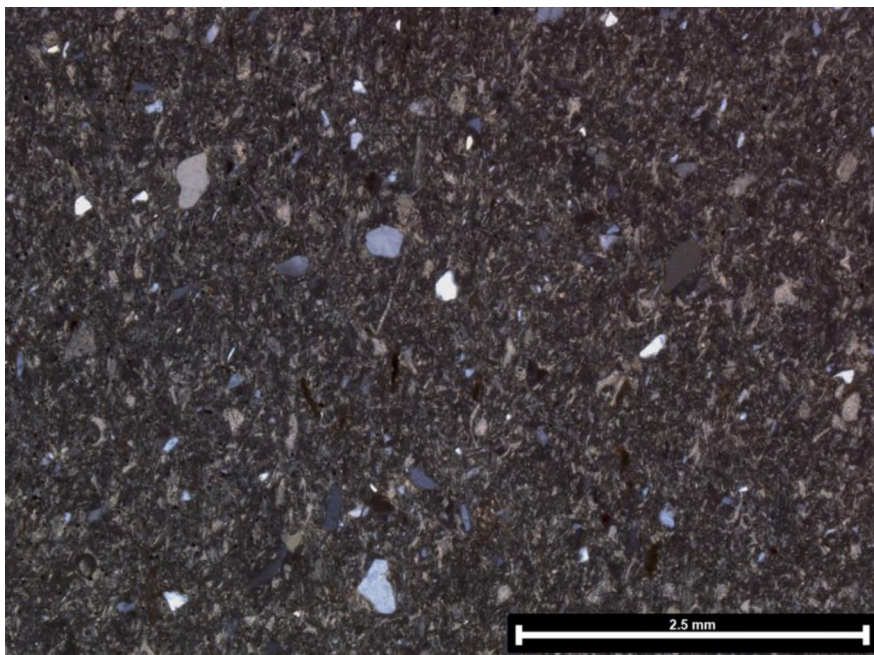
Figure A.21. Shows a cluster of anomalously rounded quartz grains. Also shows volcanic glass. Cross polarized light.

3.2.2. Sample 6-16-04.

3.2.2.1. Phases. Common phenocryst phases are small quartz and plagioclase. From this section it is fairly clear to see that the yellowish material in the groundmass is devitrified glass. Plagioclase is occasionally zoned and sieved. Accretionary lapilli are plainly seen in PPL, and consist primarily of devitrivied glass, but also contain very small crystals of quartz and plagioclase, apparent in XPL. Phenocrysts of quartz and plagioclase rarely exceed 0.5mm measured along the long axis, with most grains falling in the 0.1mm-0.3mm range. Biotite grains tend to be slightly larger, with some around 1mm along their long axis. Minor Fe-Ti oxide minerals are also present. The majority of the modal composition of the sample (>70%) is altered glass and groundmass.

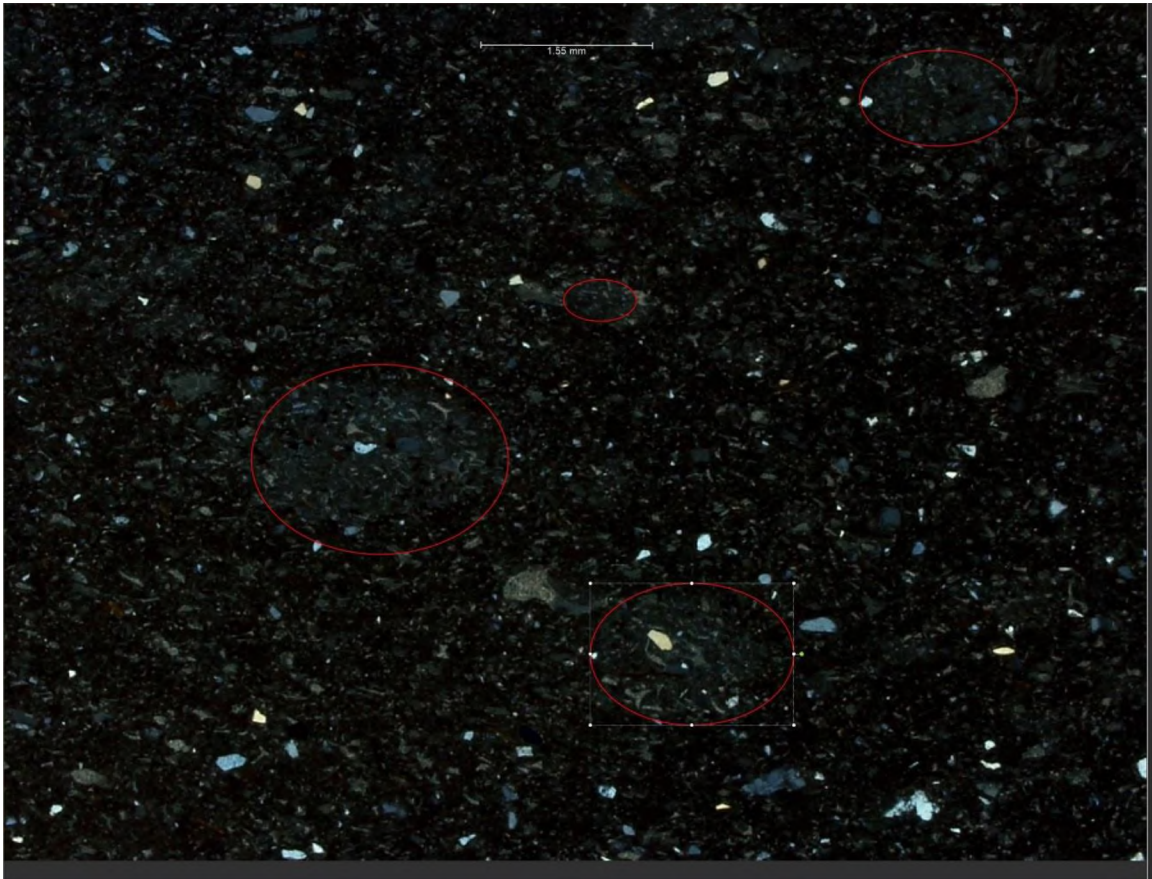Figure A.22. Reflected light image shows accretionary lapilli.

Figure A.23. Shows the same thing as above, expect in cross polarized light. Several of the lapilli are highlighted for reference. Note the broken/shattered appearance of the phenocrysts.

3.2.2.2. Textures. Plagioclase displays twinning and occasional zoning and sieving. Minerals display preferential alignment of their lsong axes perpendicular to bedding. The thin section as a whole has a shattered appearance. Crystals, where present, are small and quite angular.
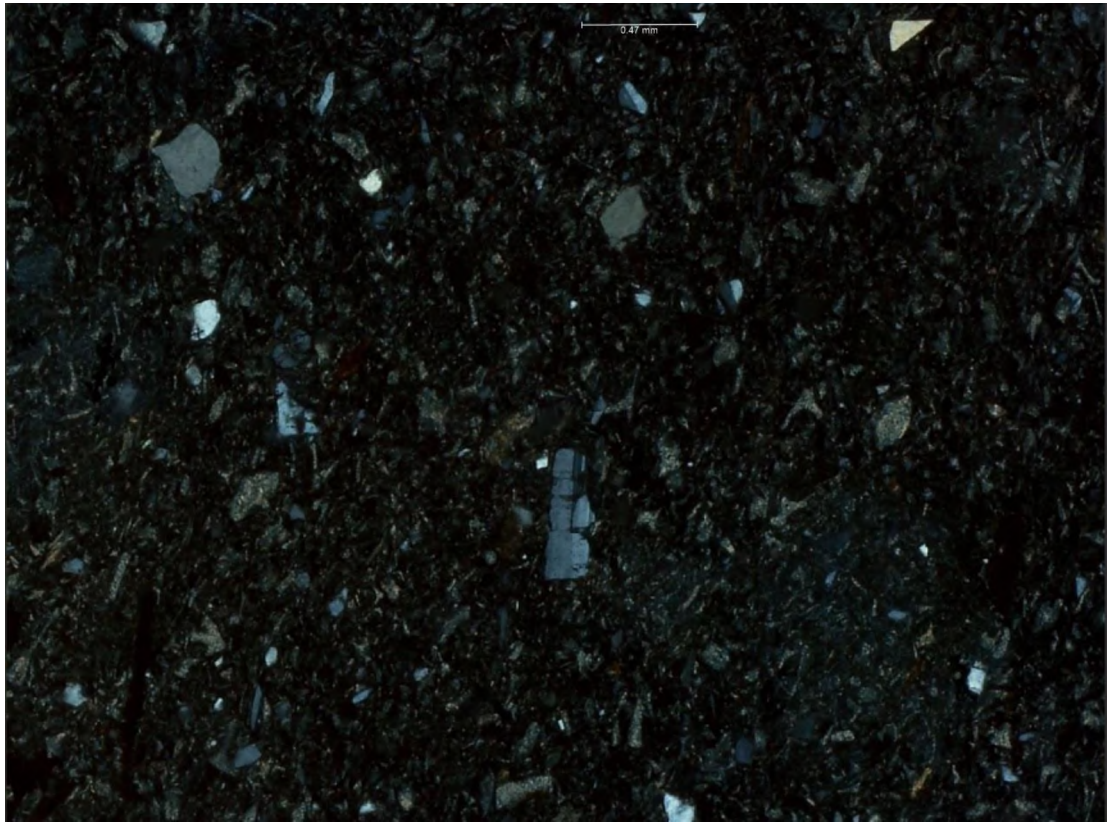
Figure A.24. Shows fragmented appearance as well as a small fragment of zoned plaigioclase, a fragment of twinned plagioclase, and altered/devitrified glass fragments. Textures present strongly imply an air fall tuff. Cross polarized light.
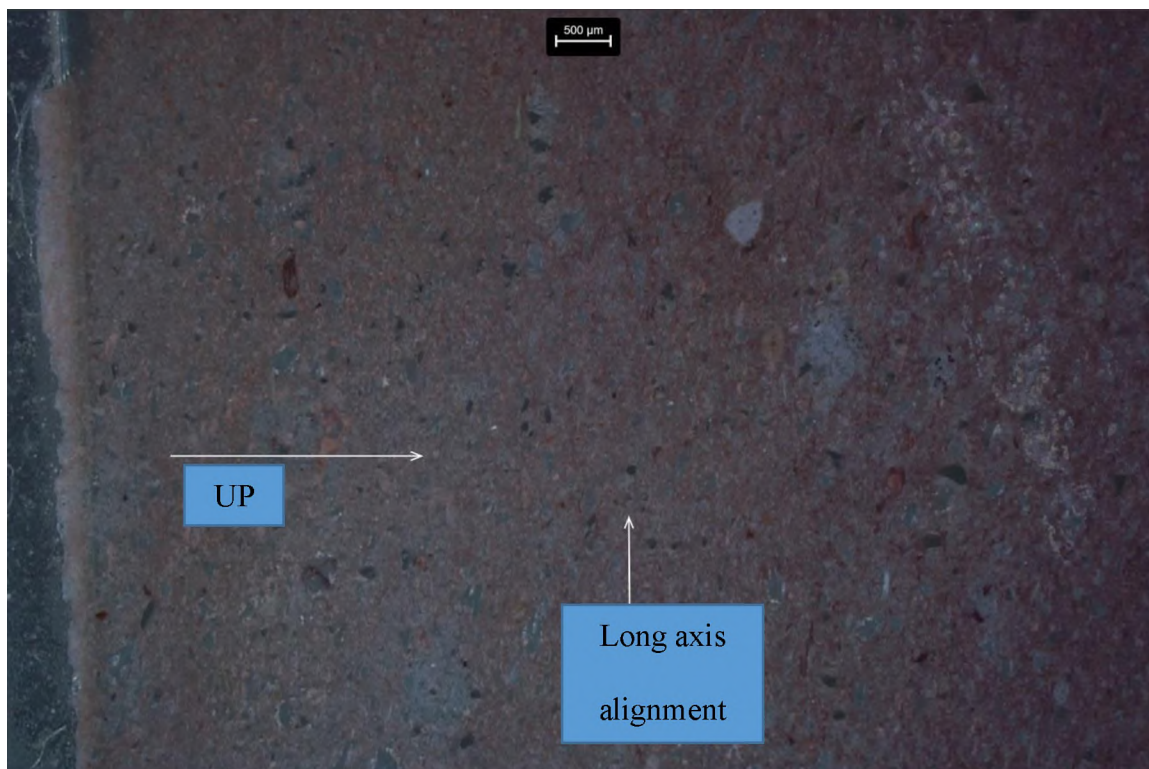
Figure A.25. Reflected light image shows the alignment of the long axis of phases perpendicular to bedding.

3.2.3. Sample 3PT-06. This sample represents the base of the tuff along the Central Creek Transect.

3.2.3.1. Phases. This sample has low crystalinity (<20%), and phenocrysts are typically small (see images below). Dominant phases include quartz and biotite. Devitrified glass shards were also noted.

3.2.3.2. Textures. Eliptical accretionary lapilli were noted in both hand sample and in thin section.
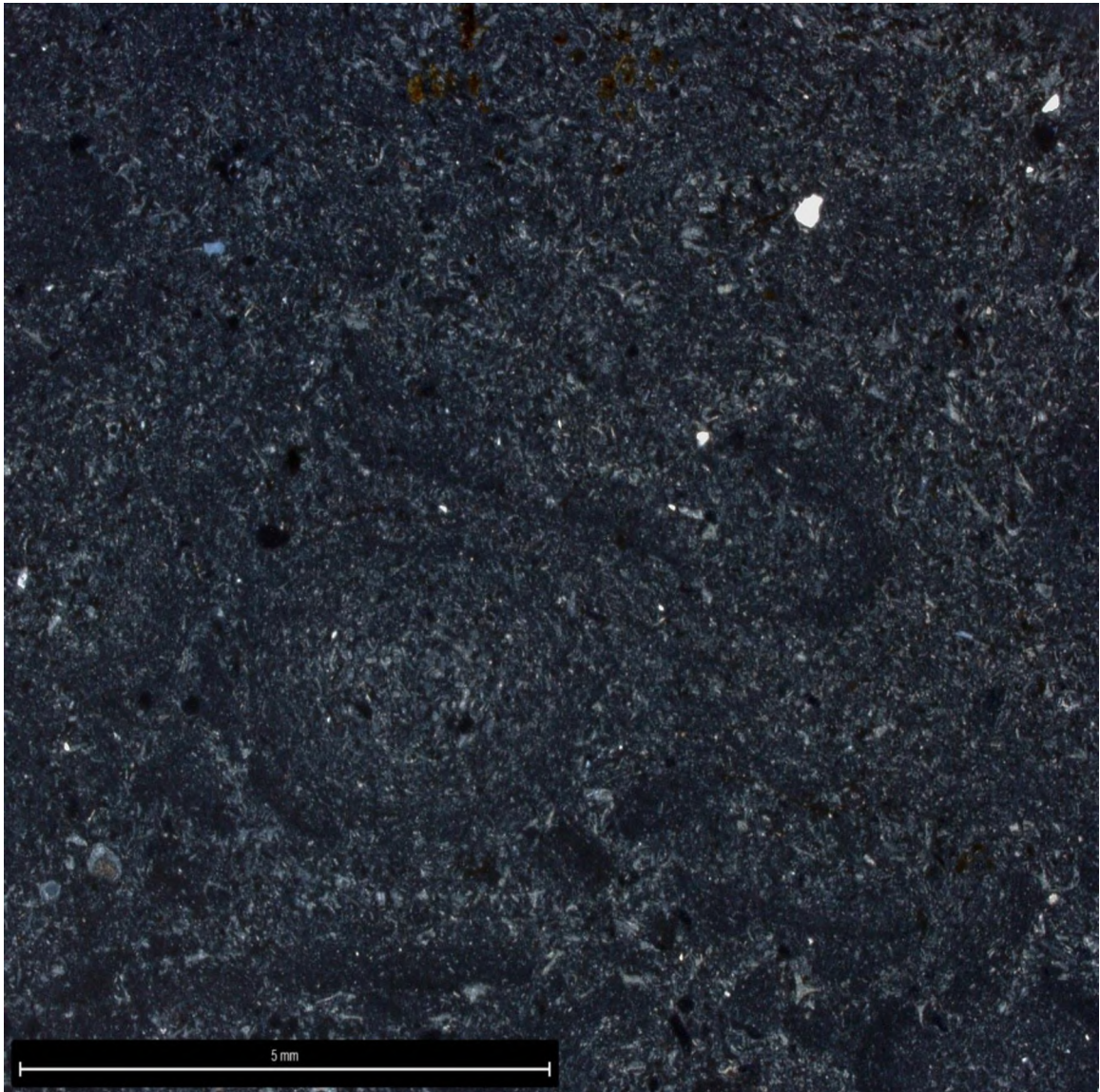
Figure A.26. Cross polarized light image of 3PT-06 showing accretionary lapilli. Small devitrified glass shards are also visible. Note the very low crystallinity.

Figure A.27. Reflected light image showing accretionary lapilli.

3.2.4. Sample 6-29-05. This sample represents the top of the Three Peaks Tuff along the Central Creek Transect. The degree of rounding of minerals present is indicative of reworking, as would be expected if an ash fall tuff were emplaced in an area of active deposition. Minerals present include quartz, and biotite.
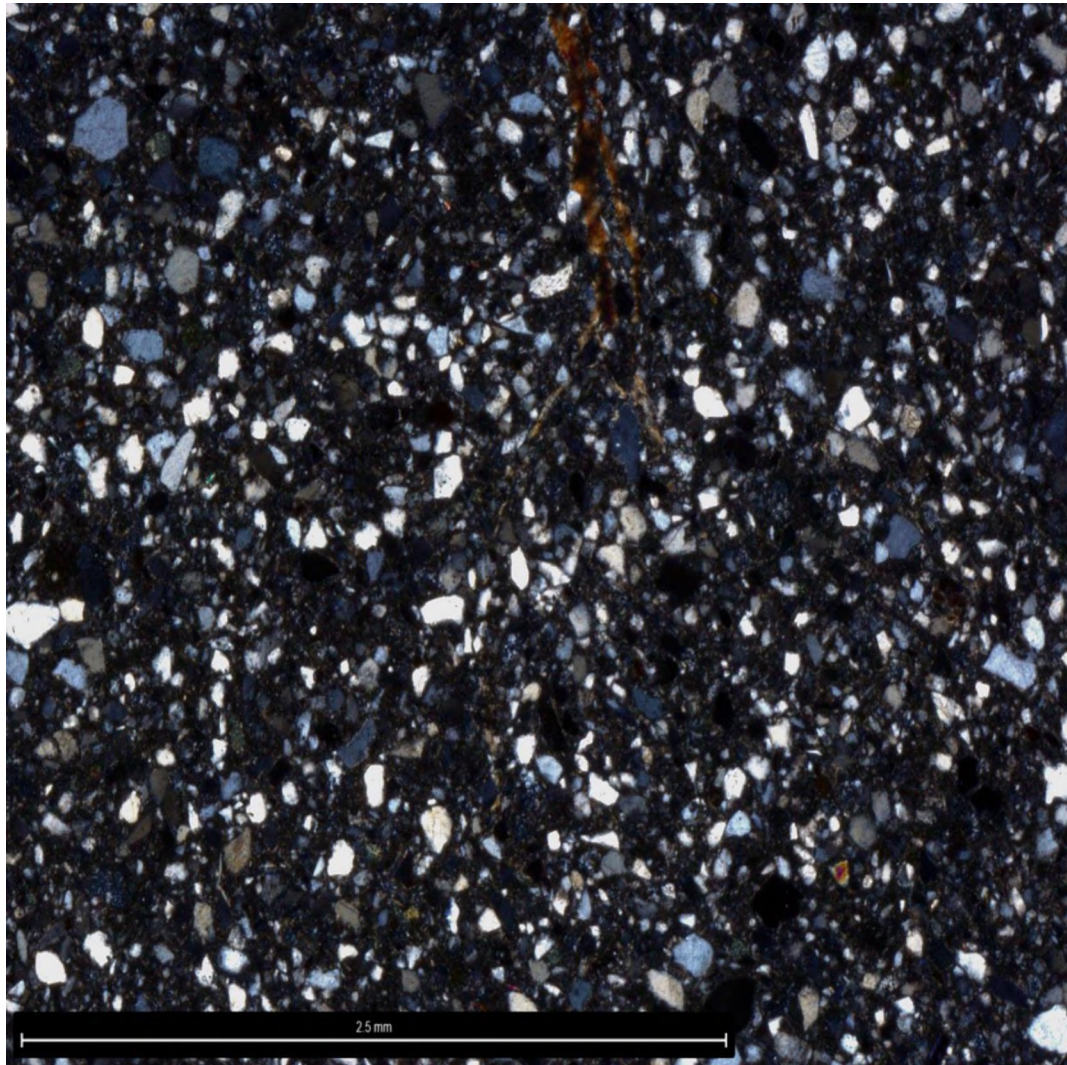
Figure A.28. The top of the Three Peaks Tuff along the Central Creek Transect.

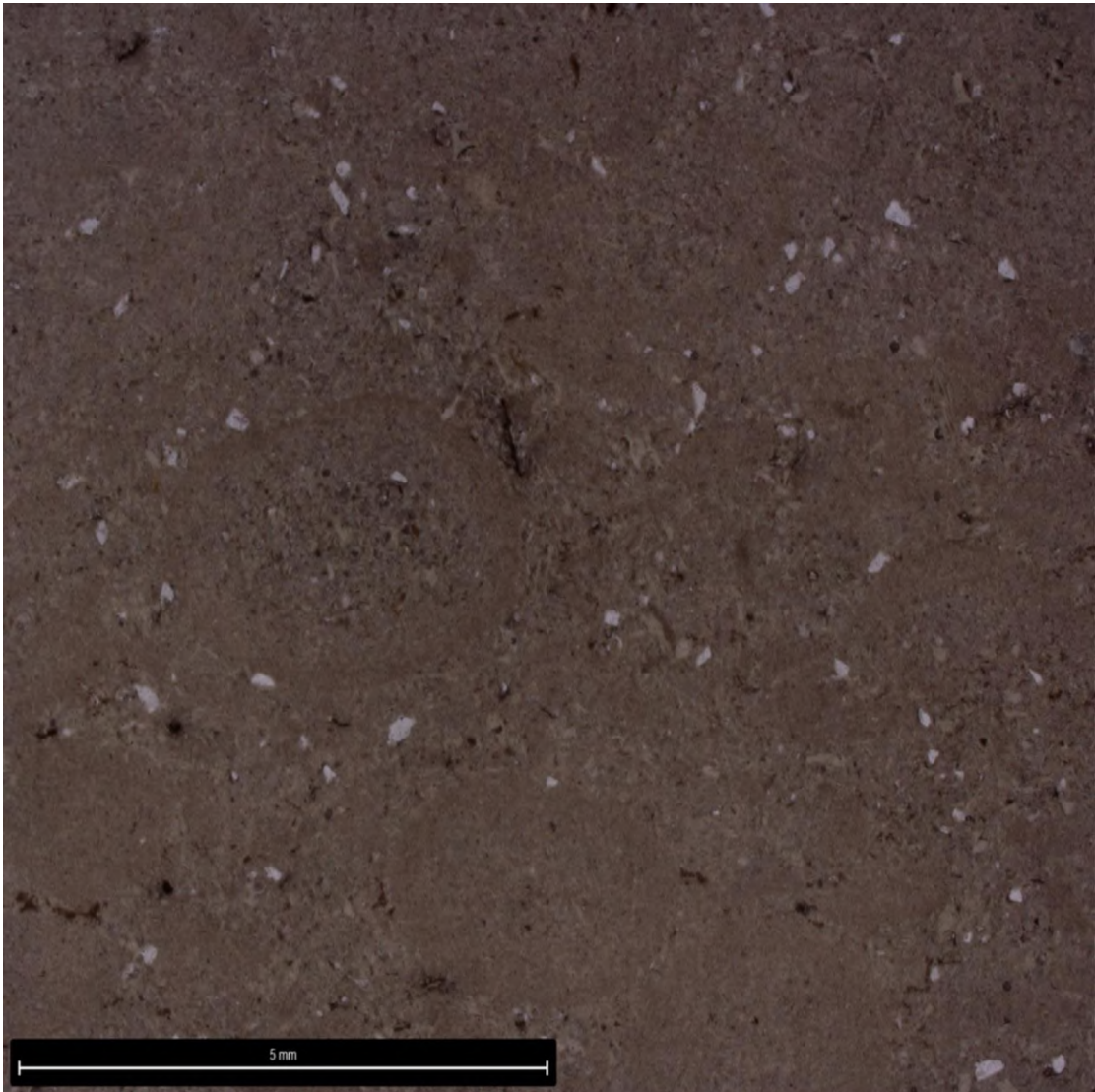**3.2.5. Sample 6-16-02.** This sample represents the base of the Three Peaks Tuff along the Shooting Range Transect.

3.2.5.1. Phases. Crystals are exceptionally small in this sample, with most well under 0.5 mm along the long axis, and consist mostly of quartz and biotite. Altered glass shards are also noted.

3.2.5.2. Textures. This sample, like several others also appears to display a preferential orientation of glass and crystals. Grains have an angular appearance.
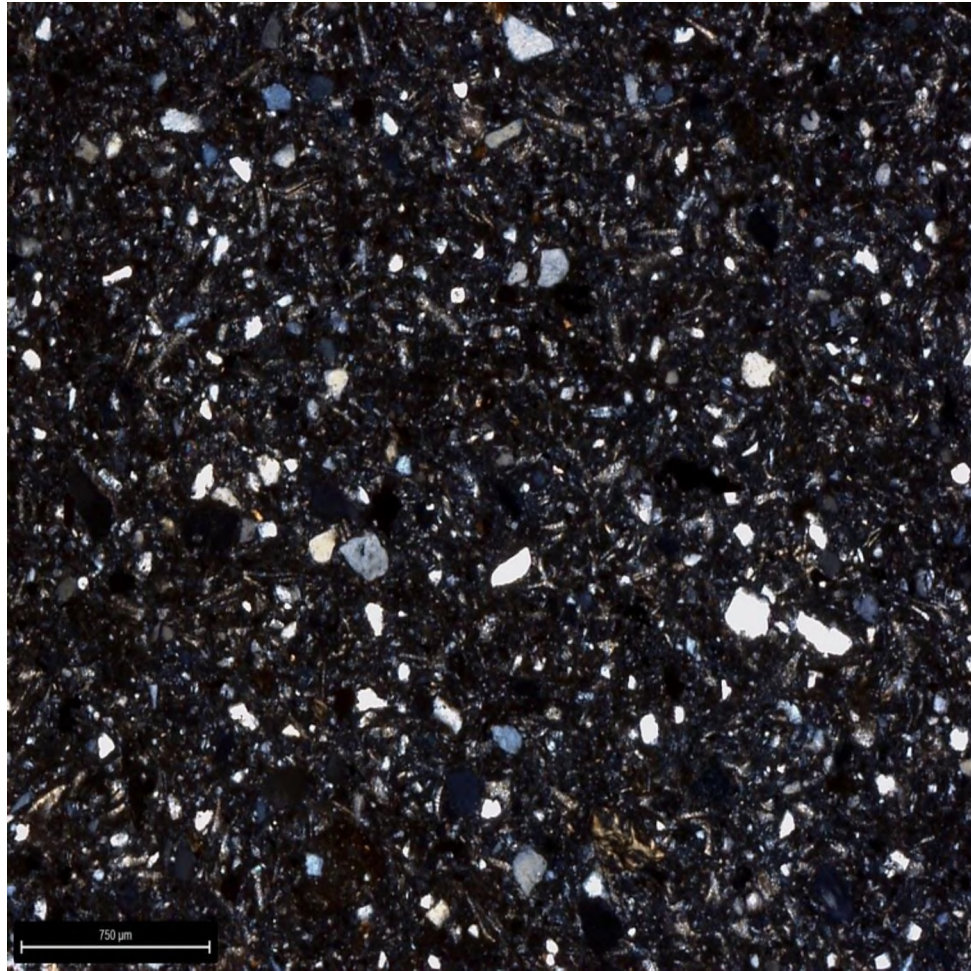
Figure A.29. Cross polarized light image of sample 6-16-02. Note how small the phenocrysts are. Devitrified glass is also present.

3.2.6. Sample 6-16-06. This sample was taken in the middle of tuff along the Shooting Range Transect.

3.2.6.1. Phenocryst phases. This sample is relatively plagioclase rich (compared to other samples examined) but is still very crystal poor. Phenocryst phases include plagioclase, quartz, and biotite. Glass shards are common. Phenocrysts rarely exceed 0.5 mm in any direction.

3.2.6.2. Textures. Grains appear to be preferentially oriented, and generally have a shattered and angular appearaence, like several samples described above. Some plagioclase appears to be altered.
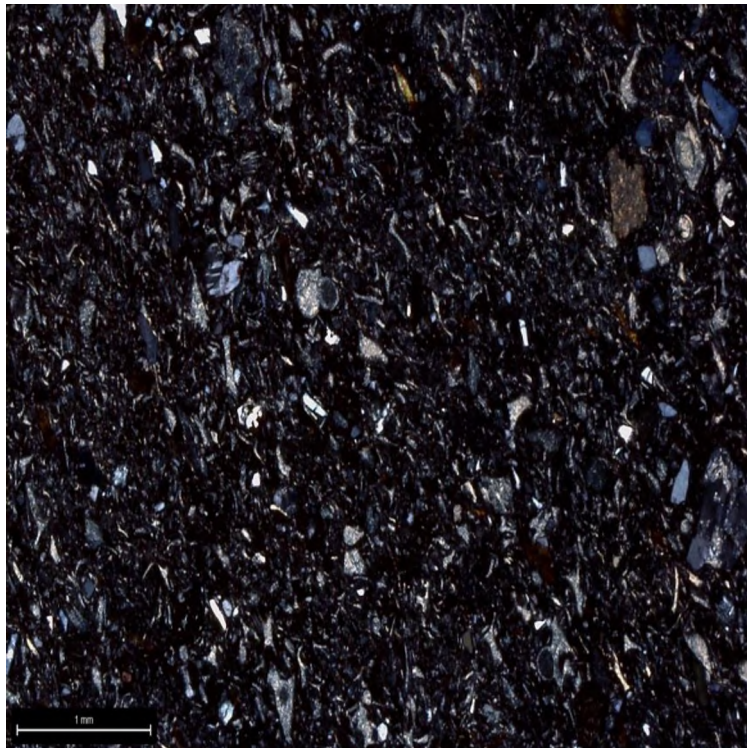
Figure A.30. Image of sample 6-16-06. Note the altered plagioclase grain in the lower right portion of the image. Cross polarized light.

3.2.7. Sample 6-16-07. This sample directly overlies 6-16-06.

3.2.7.1. Phases. Relative to 6-16-06, this sample contains more and larger biotite grains, with some of the biotite grains nearing 1mm measured across the long axis. Other dominant phases include quartz and plagioclase, which are notably smaller, rarely exceeding 0.5mm. Minor Fe-Ti oxide minerals were also noted, but relatively lower abundances. A quartzite lithic was also identified in this sample.

3.2.7.2. Textures. Plagioclase grains in this sample appear to display sieving. Grains have a shattered and angular appearance.
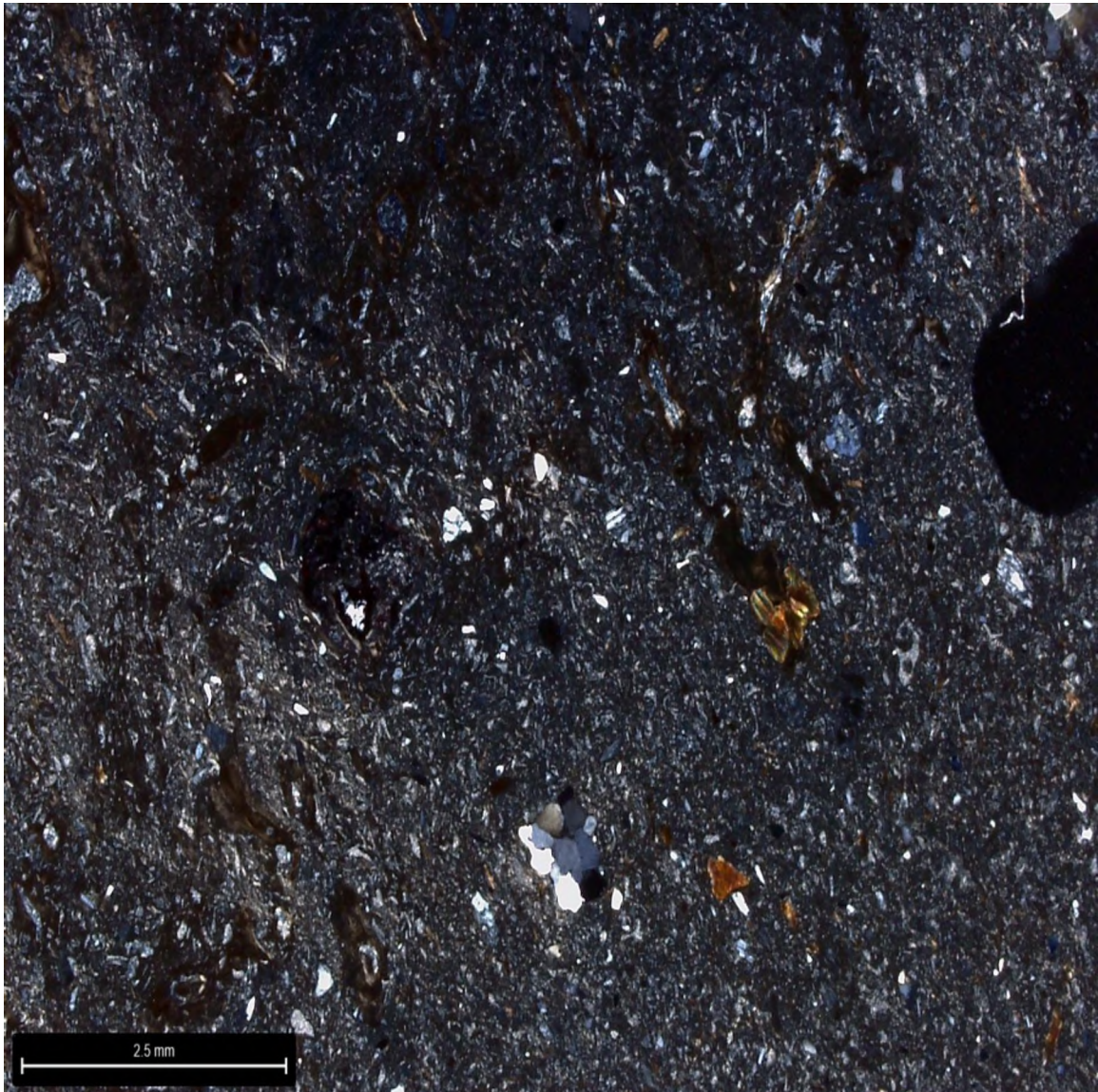
Figure A.31. Sample 6-16-07 in cross polarized light. Note the quartzite lithic in the lower center of the image. Small sieved plagioclase grains may also be seen.

3.2.8. Sample 6-16-09. This sample marks the top of the Three Peaks Tuff along the Shooting Range Traverse, and like the top of the Central Creek Traverse appears to be reworked. Dominant phases consist mostly of quartz and feldspar. Altered glass and

lapilli are conspicuously absent, while the shape of the grains is more rounded than seen

in underlying beds.
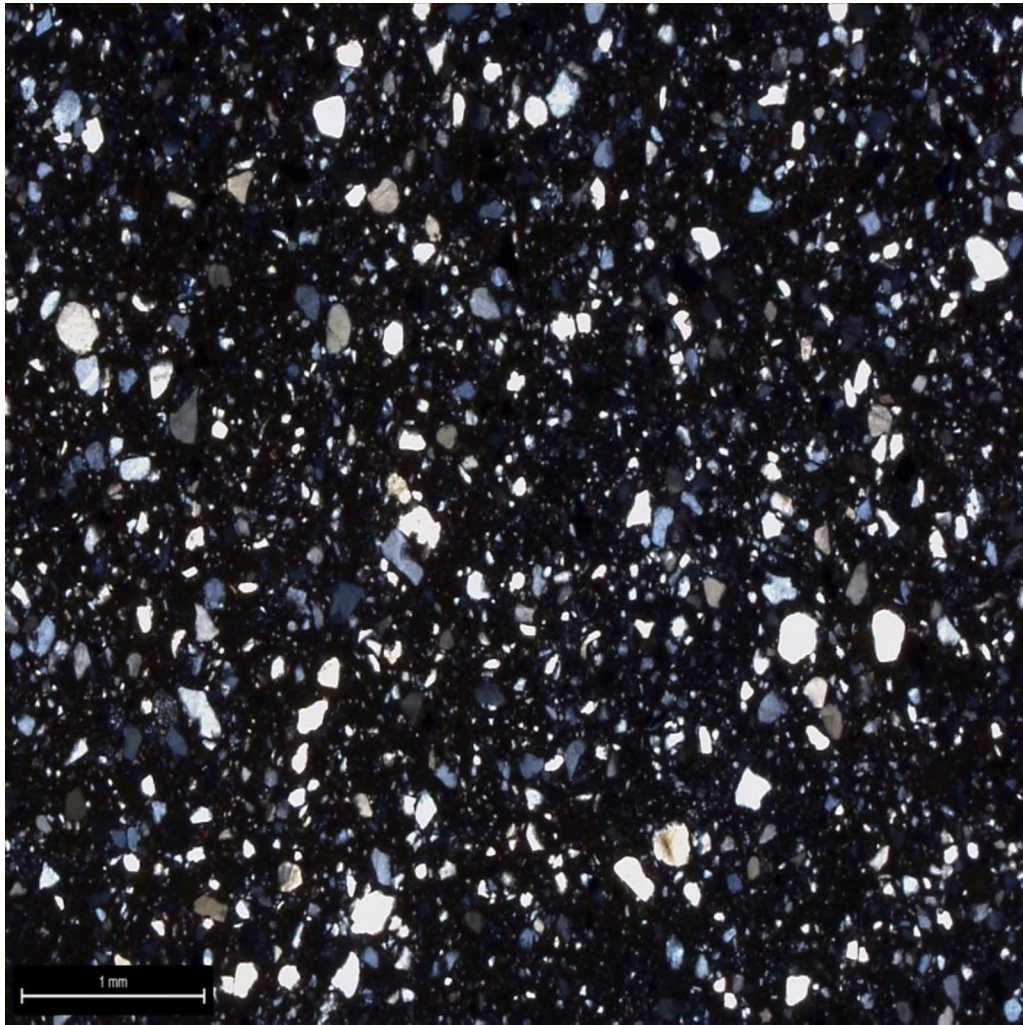
Figure A.32. Image of sample 6-16-09, marking the top of the Three Peaks Tuff along the Shooting Range Traverse. Cross polarized light.

4. LA-ICPMS METHODS

Zirocns from samples collected in the field were dated by Dr. James L. Crowley at Boise State University, according to the following methods, as reported by the laboratory at Boise State University:Zircon grains were separated from rocks using standard techniques, annealed at 900°C for 60 hours in a muffle furnace, and mounted in epoxy and polished until their centers were exposed. Cathodoluminescence (CL) images were obtained with a JEOL JSM-300 scanning electron microscope and Gatan MiniCL. Zircon was analyzed by laser ablation inductively coupled plasma mass spectrometry (LA-ICPMS) using a ThermoElectron X-Series II quadrupole ICPMS and New Wave Research UP-213 Nd:YAG UV (213 nm) laser ablation system. In-house analytical protocols, standard materials, and data reduction software were used for acquisition and calibration of U-Pb dates and a suite of high field strength elements (HFSE) and rare earth elements (REE). Zircon was ablated with a laser spot of 25 μm wide using fluence and pulse rates of 5 J/cm^2 and 5 Hz, respectively, during a 45 second analysis (15 sec gas blank, 30 sec ablation) that excavated a pit ~25 μm deep. Ablated material was carried by a 1.2 L/min He gas stream to the nebulizer flow of the plasma. Dwell times were 5 ms for Si and Zr, 200 ms for ^{49}Ti and ^{207}Pb, 80 ms for ^{206}Pb, 40 ms for ^{202}Hg, ^{204}Pb, ^{208}Pb, ^{232}Th, and ^{238}U and 10 ms for all other HFSE and REE. Background count rates for each analyte were obtained prior to each spot analysis and subtracted from the raw count rate for each analyte. Ablations pits that appear to have intersected glass or mineral inclusions were identified based on Ti and P. U-Pb dates from these analyses are considered valid if the U-Pb ratios appear to have been unaffected by the inclusions. Analyses that appear

contaminated by common Pb were rejected based on mass 204 being above baseline. For concentration calculations, background-subtracted count rates for each analyte were internally normalized to ^{29}Si and calibrated with respect to NIST SRM-610 and -612 glasses as the primary standards.

Data were collected in one experiment in September 2019. For U-Pb and ^{207}Pb/^{206}Pb dates, instrumental fractionation of the background-subtracted ratios was corrected and dates were calibrated with respect to interspersed measurements of zircon standards and reference materials. The primary standard Plešovice zircon (Sláma et al., 2008) was used to monitor time-dependent instrumental fractionation based on two analyses for every 10 analyses of unknown zircon. A secondary correction to the ^{206}Pb/^{238}U dates was made based on results from the zircon standards Seiland (530 Ma, unpublished data, Boise State University) and Zirconia (327 Ma, unpublished data, Boise State University), which were treated as unknowns and measured once for every 10 analyses of unknown zircon. These results showed a linear age bias of several percent that is related to the ^{206}Pb count rate. The secondary correction is thought to mitigate matrix-dependent variations due to contrasting compositions and ablation characteristics between the Plešovice zircon and other standards (and unknowns).

Radiogenic isotope ratio and age error propagation for all analyses includes uncertainty contributions from counting statistics and background subtraction. For groups of analyses that are collectively interpreted from a weighted mean date (i.e., igneous zircon analyses), a weighted mean date is first calculated using Isoplot 3.0 (Ludwig, 2003) using errors on individual dates that do not include a standard calibration uncertainty, and then a standard calibration uncertainty is propagated into the error on the

weighted mean date. This uncertainty is the local standard deviation of the polynomial fit to the interspersed primary standard measurements versus time for the time-dependent, relatively larger U/Pb fractionation factor, and the standard error of the mean of the consistently time-invariant and smaller $^{207}Pb/^{206}Pb$ fractionation factor. These uncertainties are 0.7% (2 sigma) for $^{206}Pb/^{238}U$ and 0.7% (2 sigma) for $^{207}Pb/^{206}Pb$. Age interpretations are based on $^{206}Pb/^{238}U$. Errors on the dates are at 2 sigma.

5. CA-TIMS U-PB GEOCHRONOLOGY METHODS

Zirocns from samples collected in the field were dated by Dr. James L. Crowley at Boise State University, according to the following methods, as reported by the laboratory at Boise State University: U-Pb dates were obtained by the chemical abrasion isotope dilution thermal ionization mass spectrometry (CA-TIMS) method from analyses composed of single zircon grains (Table 1), modified after Mattinson (2005). Zircon was separated from rocks using standard techniques, placed in a muffle furnace at 900°C for 60 hours in quartz beakers, mounted in epoxy, and polished until the centers of the grains were exposed. Cathodoluminescence (CL) images were obtained with a JEOL JSM-300 scanning electron microscope and Gatan MiniCL. Zircon was removed from the epoxy mounts for dating based on CL images.

Zircon was put into 3 ml Teflon PFA beakers and loaded into 300 $\Box$l Teflon PFA microcapsules. Fifteen microcapsules were placed in a large-capacity Parr vessel and the zircon partially dissolved in 120 microliters of 29 M HF for 12 hours at 190°C. Zircon was returned to 3 ml Teflon PFA beakers, HF was removed, and zircon was immersed in 3.5 M HNO_3, ultrasonically cleaned for an hour, and fluxed on a hotplate at 80°C for an hour. The HNO_3 was removed and zircon was rinsed twice in ultrapure H_2O before being reloaded into the 300 microliter Teflon PFA microcapsules (rinsed and fluxed in 6 M HCl during sonication and washing of the zircon) and spiked with the Boise State University mixed ^{233}U-^{235}U-^{205}Pb tracer solution (BSU1B). Zircon was dissolved in Parr vessels in 120 $\Box$l of 29 M HF with a trace of 3.5 M HNO_3 at 220°C for 48 hours, dried to fluorides, and re-dissolved in 6 M HCl at 180°C overnight. U and Pb were separated from the

zircon matrix using an HCl-based anion-exchange chromatographic procedure (Krogh, 1973), eluted together and dried with 2 μl of 0.05 N H_3PO_4.

Pb and U were loaded on a single outgassed Re filament in 5 μl of a silica-gel/phosphoric acid mixture (Gerstenberger and Haase, 1997), and U and Pb isotopic measurements made on a GV Isoprobe-T multicollector thermal ionization mass spectrometer equipped with an ion-counting Daly detector. Pb isotopes were measured by peak-jumping all isotopes on the Daly detector for 160 cycles, and corrected for 0.16 ± 0.06%/a.m.u. (2 sigma) mass fractionation. Transitory isobaric interferences due to high-molecular weight organics, particularly on ^{204}Pb and ^{207}Pb, disappeared within approximately 60 cycles, while ionization efficiency averaged 10^4 cps/pg of each Pb isotope. Linearity (to $\geq 1.4 \times 10^6$ cps) and the associated deadtime correction of the Daly detector were determined by analysis of NBS982. Uranium was analyzed as UO_2^+ ions in static Faraday mode on 10^{12} ohm resistors for 300 cycles, and corrected for isobaric interference of $^{233}U^{18}O^{16}O$ on $^{235}U^{16}O^{16}O$ with an $^{18}O/^{16}O$ of 0.00206. Ionization efficiency averaged 20 mV/ng of each U isotope. U mass fractionation was corrected using the known $^{233}U/^{235}U$ ratio of the Boise State University tracer solution.

U-Pb dates and uncertainties were calculated using the algorithms of Schmitz and Schoene (2007), $^{235}U/^{205}Pb$ of 77.93 and $^{233}U/^{235}U$ of 1.007066 for the Boise State University BSU1B tracer solution, and U decay constants recommended by Jaffey et al. (1971) and $^{238}U/^{235}U$ of 137.818 from (Hiess et al., 2012). $^{206}Pb/^{238}U$ ratios and dates were corrected for initial ^{230}Th disequilibrium using $D_{Th/U} = 0.2 \pm 0.1$ (2 sigma) and the algorithms of Crowley et al. (2007), resulting in an increase in the $^{206}Pb/^{238}U$ dates of ~0.09 Ma. All common Pb in analyses was attributed to laboratory blank and subtracted

based on the measured laboratory Pb isotopic composition and associated uncertainty. U

blanks are estimated at 0.013 ± 0.018 pg (2 sigma).

Weighted mean $^{206}Pb/^{238}U$ dates were calculated from equivalent dates

(probability of fit >0.05) using Isoplot 3.0 (Ludwig, 2003). Errors on the weighted mean

dates are given as $\pm$ x / y / z, where x is the internal error based on analytical uncertainties

only, including counting statistics, subtraction of tracer solution, and blank and initial

common Pb subtraction, y includes the tracer calibration uncertainty propagated in

quadrature, and z includes the ^{238}U decay constant uncertainty propagated in quadrature.

Internal errors should be considered when comparing our dates with $^{206}Pb/^{238}U$ dates

from other laboratories that used the same Boise State University tracer solution or a

tracer solution that was cross-calibrated using EARTHTIME gravimetric standards.

Errors including the uncertainty in the tracer calibration should be considered when

comparing our dates with those derived from other geochronological methods using the

U-Pb decay scheme (e.g., laser ablation ICPMS). Errors including uncertainties in the

tracer calibration and ^{238}U decay constant should be considered when comparing our

dates with those derived from other decay schemes (e.g., $^{40}Ar/^{39}Ar$, $^{187}Re-^{187}Os$). Errors

are given at 2 sigma.

REFERENCES

Crowley, J.L., Schoene, B., Bowring, S.A., 2007, U-Pb dating of zircon in the Bishop Tuff at the millennial scale: Geology 35: 1123-1126.

Gerstenberger, H., Haase, G., 1997, A highly effective emitter substance for mass spectrometric Pb isotope ratio determinations: Chemical Geology 136: 309-312.

Heiss, J., Condon, D.J., McLean, N., Noble, S. R., 2012, 238U/235U systematics in terrestrial uranium-bearing minerals: Science 335: 1610-1614.

Jaffey, A.H., Flynn, K.F., Glendenin, L.E., Bentley, W.C., Essling, A.M., 1971, Precision measurements of half-lives and specific activities of ^{235}U and ^{238}U: Physical Review C, 4: 1889-1906.

Krogh, T.E., 1973, A low contamination method for hydrothermal decomposition of zircon and extraction of U and Pb for isotopic age determination: Geochimica et Cosmochimica Acta 37: 485-494.

Ludwig, K.R., 2003, User's Manual for Isoplot 3.00. Berkeley Geochronology Center: Berkeley, CA, 70 p.

Mattinson, J.M., 2005, Zircon U-Pb chemical abrasion ("CA-TIMS") method: combined annealing and multi-step partial dissolution analysis for improved precision and accuracy of zircon ages: Chemical Geology 220:47-66.

Mackin, J.H., Nelson, W.H., and Rowley, P.D., compilers, 1976, Geologic map of the Cedar City Northwest Quadrangle, Iron County, Utah: U.S. Geological Survey, scale 1:24,000.

Mackin, J.H., and Rowley, P.D., compliers, 1976, Geologic map of the Three Peaks Quadrangle, Iron County, Utah: U.S. Geological Survey, scale 1:24,000.

Schmitz, M.D., Schoene, B., 2007, Derivation of isotope ratios, errors and error correlations for U-Pb geochronology using ^{205}Pb-^{235}U-(^{233}U)-spiked isotope dilution thermal ionization mass spectrometric data: Geochemistry, Geophysics, Geosystems (G^3) 8, Q08006, doi:10.1029/2006GC001492.

Sláma, J., Košler, J, Condon, D.J., Crowley, J.L., Gerdes, A., Hanchar, J.M., Horstwood, M.S.A., Morris, G.A., Nasdala, L., Norberg, N., Schaltegger, U., Schoene, B. Tubrett, M.N, Whitehouse, M.J. 2008. Plešovice zircon — A new natural reference material for U–Pb and Hf isotopic microanalysis. Chemical Geology, 249: 1-35.

APPENDIX B.

THE DEPOSITIONAL ENVIRONMENT OF THE MARSHALL CREEK BRECCIA DISCUSSED IN DETAIL: HOW IS IT RELATED TO NEARBY THRUST FAULTING?

The depositional environment of the Marshall Creek breccia has been debated in the literature. Early investigators postulated an origin as a fanglomerate-mudflow breccia and talus as part of alluvial debris flow derived from the uplifted Co-op Creek Limestone member (Mackin, 1947; Mackin and Rowley, 1976; Fillmore, 1991). Knudsen and Biek (2014), based upon stratigraphic similarities to the lowermost Iron Springs formation, interpret the clasts as intraformational rip-up clasts and, in conjunction with soft-sediment deformation, conclude the Marshall Creek breccia to represent subaqueous slide deposits triggered by deformation due to nearby Sevier faulting. In addition, based on stratigraphic relationships, they suggest that the Marshall Creek breccia and lowermost Iron Springs were both deformed prior to lithification, and that the Marshall Creek breccia should be included with the Iron Springs Formation. Our field observations confirm the presence of intraformational rip-up clasts in limestone beds that occur in the Iron Springs Formation stratigraphically above the Marshall Creek Breccia. However, our field observations support Fillmore's (1991), Mackin's (1947), and Mackin and Rowley's (1976) interpretation that the Marshall Creek breccia consists of clasts mostly derived from the Co-op Creek Limestone Member of the Jurassic Carmel Formation. The Co-op Creek Limestone and the clasts of the Marshall Creek are both light to dark grey Dunham mudstone, and appear indistinguishable in hand sample. Further, while many of the limestone clasts are very angular, some of the limestone clasts are rounded to subrounded (Supplementary Fig. 2), a physical characteristic much more likely to develop in an alluvial setting. Measured sections demonstrate the Marshall Creek breccia locally interfingers with the basal conglomerate of the lower Iron Springs over a stratigraphic interval of approximately 18 meters, supporting Knudsen and Biek's (2014) suggestion

that this unit be included with the Iron Springs Formation. Given the field relationships mentioned, we interpret the Marshall Creek breccia to have been deposited as large talus blocks eroded from the Co-op Creek Limestone, which is uplifted in the hanging wall of the Iron Springs Thrust (Mackin et al., 1976; Knudsen and Biek, 2014) and exposed at the southernmost extent of the breccia. Limestone talus was transported short distances as debris flow, interspersed with mudflows as part of a fanglomerate and alluvial fan system (e.g., Ribes et al., 2019; Laird and Hope, 1968). Between debris and mudflow events, sediment was supplied to the alluvial system by streams carrying quartzite and limestone eroded from bedrock uplifted by the Wah Wah Thrust (Fillmore, 1991). Most significantly, we concur with Knudsen and Biek (2014), agreeing that the Marshall Creek breccia and the lowermost Iron Springs Formation record syndepositional deformation related to movement on nearby thrust faults associated with the Sevier front. Additionally, the Iron Springs Thrust locally places Co-op Creek Limestone member of the Carmel Formation over deformed and locally overturned Iron Springs Formation, Marshall Creek breccia, and Crystal Creek Member of the Carmel Formation in the footwall of the fault (Mackin and Rowley, 1976; Knudsen and Biek, 2014). This demonstrates that the Marshall Creek breccia and Iron Springs Formation were deposited during and prior to cessation of movement along the Iron Springs Thrust, hinting that the Iron Springs Thrust system was active for a relatively long period of time.

REFERENCES

Laird, M.G., and Hope, J.M., 1968, The Torea Breccia and the Papahaua Overfold: New Zealand Journal of Geology and Geophysics, v. 11, p. 418-34. https://doi: 10.1080/00288306.1968.10423660.

Fillmore, R.P., 1991, Tectonic influence on sedimentation in the southern Sevier foreland, Iron Springs Formation (Upper Cretaceous), southwestern Utah, in Nations, J.D., and Eaton, J.G., eds., Stratigraphy, depositional environments; and sedimentary tectonics of the western margin, Cretaceous Western Interior Seaway: Geological Society of America Special Paper 260, p. 9-25.

Knudsen, T.R., and Biek, R.F., compilers, 2014, Interim geologic map of the Cedar City NW Quadrangle, Iron County, Utah: Utah Geological Survey open file report 627, scale 1:24,000.

Mackin, J.H., Nelson, W.H., and Rowley, P.D., compilers, 1976, Geologic map of the Cedar City Northwest Quadrangle, Iron County, Utah: U.S. Geological Survey, scale 1:24,000.

Mackin, J.H., and Rowley, P.D., compliers, 1976, Geologic map of the Three Peaks Quadrangle, Iron County, Utah: U.S. Geological Survey, scale 1:24,000.

Mackin, J.H., 1947, Some structural features in the intrusions in the Iron Springs district: Guidebook to the geology of Utah, no. 2: Utah Geological Society, 62 p.

Fillmore, R.P., 1991, Tectonic influence on sedimentation in the southern Sevier foreland, Iron Springs Formation (Upper Cretaceous), southwestern Utah, in Nations, J.D., and Eaton, J.G., eds., Stratigraphy, depositional environments; and sedimentary tectonics of the western margin, Cretaceous Western Interior Seaway: Geological Society of America Special Paper 260, p. 9-25.

Ribes, C., Ghienne, J.-F., Manatschal, G., Decarlis, A., Karner, G.D., Figueredo, P.H., and Johnson, C.A., 2019, Long-lived mega fault-scarps and related breccias at distal rifted margins: Insights from continental rifted margin and fossil analogues: Journal of the Geological Society [London], v. 176, no. 5, p. 801–816, https://doi: 10.1144/jgs2018-181.

BIBLIOGRAPHY

Ardila, A.M., Paterson, S.R., Memeti, V., Parada, M.A., and Molina, P.G., 2019, Mantle driven Cretaceous flare-ups in Cordilleran arcs: Lithos, v. 326–327, p. 19–27, https://doi: 10.1016/j.lithos.2018.12.007.

Barker, D.S., 1995, Crystallization and alteration of quartz monzonite, Iron Springs mining District, Utah: Relation to associated iron deposits: Economic Geology, v. 90, p. 2197–2217.

DeCelles, P.G., and Graham, S.A., 2015, Cyclical processes in the North American Cordilleran orogenic system: Geology, v. 43, p. 499–502, https://doi:10.1130/G36482.1.

DeCelles, P.G., 2004, Late Jurassic to Eocene evolution of the Cordilleran thrust belt and foreland basin systems, western USA: American Journal of Science, v. 304, p. 105–168, https://doi:10.2475/ajs.304.2.105.

DeCelles, P.G., 1994, Late Cretaceous–Paleocene synorogenic sedimentation and kinematic history of the Sevier thrust belt, northeast Utah and southwest Wyoming: Geological Society of America Bulletin, v. 106, p. 32–56, https://doi:10.1130/0016-7606(1994)106<0032:LCPSSA>2.3.CO;2.

Fillmore, R.P., 1991, Tectonic influence on sedimentation in the southern Sevier foreland, Iron Springs Formation (Upper Cretaceous), southwestern Utah, in Nations, J.D., and Eaton, J.G., eds., Stratigraphy, depositional environments; and sedimentary tectonics of the western margin, Cretaceous Western Interior Seaway: Geological Society of America Special Paper 260, p. 9-25.

Fleck, R.J., and Carr, M.D., 1990, The age of the Keystone thrust: Laser-fusion 40Ar/39Ar dating of foreland basin deposits, southern Spring Mountains, Nevada: Tectonics, v. 9, p. 467-476.

Giallorenzo, M., Wells, M.L., Yonkee, W.A., Stockli, D.F., and Wernicke, B.P., 2018, Timing of exhumation, Wheeler Pass thrust sheet, southern Nevada and California: Late Jurassic to middle Cretaceous evolution of the southern Sevier fold-thrust belt: Geological Society of America Bulletin, v. 130, p. 558–579, https://doi:10.1130/B31777.1.

Knudsen, T.R., and Biek, R.F., compilers, 2014, Interim geologic map of the Cedar City NW Quadrangle, Iron County, Utah: Utah Geological Survey open file report 627, scale 1:24,000.

Yonkee, A., and Weil, A.B., 2015, Tectonic evolution of the Sevier and Laramide belts within the North American Cordillera orogenic system: Earth-Science Reviews, v. 150, p. 531–593, https://doi: 10.1016/j.earscirev.2015.08.001.

VITA

James Daniel Quick graduated *summa cum laude* from Missouri State University in Springfield, MO with a Bachelor of Science in Geology in December 2018. In December 2020, he graduated with a Master of Science in Geology and Geophysics from Missouri University of Science and Technology.